The Astrophysical Journal, 974:16 (21pp), 2024 October 10 https://doi.org/10.3847/1538-4357/ad67dc

The Black Hole Mass and Photometric Components of NGC 4826

Kayhan Gültekin[1], Karl Gebhardt[2], John Kormendy[2,3], Adi Foord[4], Ralf Bender[3,5], Tod R. Lauer[6], Jason Pinkney[7], Douglas O. Richstone[1], and Scott Tremaine[8,9]
[1] Department of Astronomy, University of Michigan, 1085 S University Avenue, Ann Arbor, MI 48109, USA; kayhan@umich.edu
[2] Department of Astronomy, University of Texas, Austin, TX 78712, USA
[3] Max Planck Institute for Extraterrestrial Physics, Giessenbachstrasse, D-85748 Garching by Munich, Germany; rzoeller@mpe.mpg.de
[4] Department of Physics, University of Maryland Baltimore County, 1000 Hilltop Circle, Baltimore, MD 21250, USA
[5] University Observatory, Faculty of Physics, Ludwig-Maximilians-Universität München, Scheinerstraße 1, 81679 Munich, Germany
[6] NSF National Optical Infrared Astronomy Research Laboratory, Tucson, AZ 85726, USA
[7] Ohio Northern University, School of Science, Technology, and Mathematics, 525 S. Main Street, Ada, OH 45810, USA
[8] School of Natural Sciences, Institute for Advanced Study, 1 Einstein Drive, Princeton, NJ 08540, USA
[9] Canadian Institute for Theoretical Astrophysics, University of Toronto, 60 St. George Street, Toronto, ON M5S 3H8, Canada
Received 2024 January 16; revised 2024 July 9; accepted 2024 July 22; published 2024 October 1

Abstract

We present infrared photometry and Hubble Space Telescope imaging and spectroscopy of the Sab galaxy NGC 4826. Schwarzschild dynamical modeling is used to measure its central black hole mass M. Photometric decomposition is used to enable a comparison of M to published scaling relations between black hole masses and properties of host bulges. This decomposition implies that NGC 4826 contains classical and pseudobulges of approximately equal mass. The classical bulge has best-fit Sérsic index $n = 3.27$. The pseudobulge is made up of three parts, an inner lens ($n = 0.18$ at $r \lesssim 4''$), an outer lens ($n = 0.17$ at $r \lesssim 45''$), and a $n = 0.58$ Sérsic component required to match the surface brightness between the lens components. The total V-band luminosity of the galaxy is $M_{VT} = -21.07$, the ratio of classical bulge to total light is $B/T \simeq 0.12$, and the ratio of pseudobulge to total light is $PB/T \simeq 0.13$. The outer disk is exponential ($n = 1.07$) and makes up $D/T = 0.75$ of the light of the galaxy. Our best-fit Schwarzschild model has a black hole mass with 1σ uncertainties of $M = 8.4^{+1.7}_{-0.6} \times 10^6\ M_\odot$ and a stellar population with a K-band mass-to-light ratio of $\Upsilon_K = 0.46 \pm 0.03\ M_\odot L_\odot^{-1}$ at the assumed distance of 7.27 Mpc. Our modeling is marginally consistent with $M = 0$ at the 3σ limit. These best-fit parameters were calculated assuming the black hole is located where the velocity dispersion is largest; this is offset from the maximum surface brightness, probably because of dust absorption. The black hole mass—one of the smallest measured by modeling stellar dynamics—satisfies the well known correlations of M with the K-band luminosity, stellar mass, and velocity dispersion of the classical bulge only. In contrast, the black hole is undermassive with respect to the correlation of M with total (classical plus pseudo) bulge luminosity. Thus the composite (classical bulge plus pseudobulge) galaxy NGC 4826 is consistent with previous results on black hole scaling relations and helps to strengthen these results at low black hole masses.

Unified Astronomy Thesaurus concepts: Black holes (162); Galaxy bulges (578); Galaxy structure (622); Scaling relations (2031)

1. Introduction

NGC 4826 (M64) has been called the "Evil Eye Galaxy" (Braun et al. 1992), the "Black Eye Galaxy" (van Driel & Buta 1993), and the "Sleeping Beauty Galaxy" (Rubin 1994) on account of its prominent and beautiful dust lanes. Its morphological classification is Sab(s) (Sandage & Bedke 1994), and it is an isolated galaxy with counter-rotating gas disks (Braun et al. 1992; van Driel & Buta 1993).

Because of its proximity, NGC 4826 is an excellent galaxy to test ideas about low-mass black holes in galaxies. It is well established that black hole mass M scales with host galaxy spheroid properties such as effective velocity dispersion (σ_e; Ferrarese & Merritt 2000; Gebhardt et al. 2000a) and luminosity ($L_{\rm bulge}$; Dressler 1989; Kormendy 1993a; Kormendy & Richstone 1995). In contrast, the scaling of M with pseudobulge properties and total luminosity in disk galaxies is more uncertain (Kormendy & Ho 2013a; Reines & Volonteri 2015). Black holes in galaxies with pseudobulges tend to be undermassive compared to black holes in galaxies with similar-luminosity classical bulges (Hu 2008; Greene et al. 2010; Kormendy et al. 2011; Kormendy & Ho 2013a; Reines & Volonteri 2015; Savorgnan et al. 2016). Also (see the above references), the distribution of their black hole masses is almost certainly the upper envelope of a distribution that extends to smaller black hole masses. Understanding the evolution and demographics of low-mass black holes and of black holes in pseudobulges is important in part because these black holes are closest in mass to the initial, "seed" black holes that grew via galaxy mergers and AGN-driving gas accretion into the giant black holes that we see in giant classical bulges and elliptical galaxies. Therefore, measurements of their masses put constraints on black hole formation models.

The demographics of low-mass black holes are also important for space-based gravitational wave experiments such as the Laser Interferometer Space Antenna (LISA), which are most sensitive to gravitational wave frequencies produced by binary black holes with total mass $\sim 10^5$–$10^7\ M_\odot$ (Amaro-Seoane et al. 2023). The number density of black holes in this mass range is poorly constrained because of the relative lack of

direct dynamical mass measurements. There are a number of measurements of small black hole masses using maser observations (Kuo et al. 2011; Greene et al. 2016). The distribution of black hole masses from this sample pushes down to much smaller masses than is expected from their velocity dispersions and the M–σ relation. The undermassive black holes were shown by Kormendy & Ho (2013a) to be either hosted by pseudobulges or in galaxies classified as "mergers in progress."

The details of the evolution of black holes in pseudobulges are not well understood. It has been thought that black holes can be fed through the same secular processes that make pseudobulges—the rearrangement of disk angular momentum by bars, globally oval disks, and (in certain cases) global spiral structure. These can form outer, inner, and nuclear rings; they can increase the central stellar mass concentration in pseudobulges (thereby possibly destroying any bar), and they may feed AGNs (see Kormendy 1993b, 2013 and, e.g., Kormendy & Kennicutt 2004 for reviews). In galaxies that contain both a classical and a pseudobulge (such as NGC 4826, Section 2.3), the situation is likely more complicated. In particular, we argue here that accretion of a gas-rich dwarf galaxy—not the more classic kind of secular evolution—may have built the galaxy's pseudobulge. Cataloging the population of low-mass black holes and the population of black holes in pseudobulges is necessary to make progress.

In this paper, we analyze NGC 4826 as a nearby galaxy with a small stellar bulge to probe the demographics of black holes in such hosts. There is a wealth of space-based imaging and spectroscopic data to work with. NGC 4826 was observed as part of Hubble Space Telescope (HST) programs GO-8591 (PI: D. O. Richstone) with Wide Field Planetary Camera 2 (WFPC2) and Space Telescope Imaging Spectrograph (STIS). It was also observed with the Hobby–Eberly Telescope Low Resolution Spectrograph. We combined these data sets with public observatory databases for our analysis.

Section 2 is a description of the imaging observations and photometric decomposition. Section 3 describes the spectroscopic observations and analysis required for modeling. We describe our kinematic modeling and black hole mass estimation results of these data in Section 4. We discuss our results, including the multiwavelength analysis of NGC 4826's nucleus and comparison of the black hole mass to scaling relations in Section 5. Finally, we summarize our results in Section 6.

Throughout this paper, we assume that the distance to NGC 4826 is $D = 7.27$ Mpc (as in Kormendy & Ho 2013a, 2013b) from surface brightness fluctuations (Tonry et al. 2001, corrected via Blakeslee et al. 2009). All distance-dependent quantities are scaled to this value.

1.1. Classical Bulges and Galaxy Mergers; Pseudobulges and Galaxy Secular Evolution

We emphasize that classical bulges and pseudobulges are defined purely by observational properties and that our understanding of their evolution is separate from the black hole detection and mass measurement presented in this paper. However, it is revealed in Section 5.2 that our observational conclusions about correlations (or not) of the NGC 4826 black hole with its host galaxy components reinforce our understanding of the relationships between morphological components and galaxy evolution.

Classical bulges were originally defined (e.g., Sandage 1961) as, in essence, elliptical galaxies that live in the middle of a galaxy disk. Ellipticals (E) were characterized as having essentially elliptical isophotes, much higher central surface brightnesses than their associated disks, steep brightness gradients, and old stellar populations. At that time, it was thought that bulges and ellipticals had surface brightness profiles $I(r)$ described by the de Vaucouleurs (1959) "$r^{1/4}$ law" that brightness depends on radius r as $\log I \propto r^{1/4}$. Modern work calls for refinement in this definition (see Kormendy et al. 2009 for a review): both bulges and ellipticals have surface brightness profiles that are well described by Sérsic (1968) functions such that $\log I \propto r^{1/n}$, where the Sérsic index is generally different from the de Vaucouleurs value $n = 4$. Experience (again see Kormendy et al. 2009) tells us the classical bulges and elliptical galaxies with absolute magnitudes $M_V \gtrsim -21.6$ mostly have Sérsic index $1.8 \lesssim n \lesssim 4$, whereas ellipticals with $M_V \lesssim -21.6$ generally have $n \gtrsim 4$.

One further important addition is necessary for the definition of both ellipticals and classical bulges: in order to be so classified, they need to satisfy the E + classical bulge "fundamental plane" structural parameter correlations between the effective radius r_e that contains $1/2$ of the light of the component, effective surface brightness μ_e at r_e, velocity dispersion σ, and absolute magnitude M_V (e.g., Djorgovski & Davis 1987; Faber et al. 1987; Dressler et al. 1987; Djorgovski et al. 1988; Djorgovski 1992; Bender et al. 1992, 1993) or its projections. The reason is that another kind of galaxy—usually called a "spheroidal" (Sph) or "dwarf elliptical" galaxy—also satisfies the purely descriptive morphology of elliptical galaxies but proves to have very different structural parameter correlations and, it turns out, different formation histories (e.g., Wirth & Gallagher 1984; Kormendy 1985, 1987; Kormendy & Bender 2009, 2012). This latter point is the reason why we check our bulge–pseudobulge–disk decomposition parameters in the Appendix.

We also need to emphasize that elliptical galaxies are intrinsically much less flattened than disks; they have intrinsic ellipticities of E0–E5 (Sandage et al. 1970; Binney & de Vaucouleurs 1981). Elliptical galaxies and classical bulges also show other features; e.g., the isophotes of elliptical galaxies can be distorted by a few percent in radius to be slightly "more disky" (equatorially flattened) or "more boxy" than exactly elliptical isophotes. These details are not relevant here. For the purposes of this paper, we can consider a classical bulge to be essentially indistinguishable from an elliptical galaxy of the same luminosity.

So far, we have said nothing about formation processes. However, galaxy evolution has been studied in detail, and those studies add refinement to the above definitions. A large body of work—observational, theoretical, and numerical simulation—has established with some confidence (although not without continuing debate) that elliptical galaxies and the classical bulges of disk galaxies formed via major mergers of two or more galaxies (or a series of such mergers) in which cold gas dissipation did not produce a disk component in the merger remnant. By "major," we mean that the stellar mass ratio of the merger progenitors was $\gtrsim 1/4$. Either or both merger progenitors may have been an elliptical already or may have contained a classical bulge. But the important refinement that helps us here is this: When the merger progenitor(s) contained a substantial outer disk component, the merger scrambles it into

an elliptical galaxy with Sérsic index ∼2–3. We know of no numerical simulation that produced an elliptical galaxy or classical bulge with $n \ll 2$. We adopt this picture of galaxy evolution and will use the result that classical bulges do not have $n \ll 2$. This paragraph summarizes a large volume of literature; the idea that mergers make ellipticals originates with Toomre (1977), and a very partial list of reviews includes Kormendy & Djorgovski (1989), de Zeeuw & Franx (1991), Barnes & Hernquist (1992), and Cappellari (2016). A revealing numerical simulation in which the preexisting disks in a major merger produce an elliptical galaxy with $n < 4$ is Mihos & Hernquist (1994).

The foregoing discussion of classical bulges is necessary in order to understand the definition and importance of pseudobulges.

Whereas observations and galaxy-evolution theory progressed together and influenced each other, it is important to realize that the galaxy components now known as "pseudobulges" were first recognized observationally (Kormendy 1979, 1981, 1993b). Pseudobulges can be—and, for the purposes of this paper, are—defined purely observationally. The classification criteria that are most important here are that pseudobulges are more disk-like than classical bulges. In particular, they are flatter. Also, rotation is more important in comparison to random motions than in classical bulges, and in many cases, their stellar velocity dispersions are smaller than the ridge line and scatter in the Faber & Jackson (1976) correlation between σ and M_V. Furthermore, except in S0 galaxies, pseudobulges frequently contain cold gas and active star formation. Criteria for recognizing pseudobulges are listed in Kormendy & Kennicutt (2004), Fisher & Drory (2011), and Kormendy (2013, 2016). Pseudobulges that have been studied in detail have brightness profiles that are well described by Sérsic functions, with one classification criterion that we particularly use here: they can have Sérsic indices $n \ll 2$. Exponential ($n = 1$) brightness profiles or ones with even stronger outer cutoffs ($n < 1$) are common.

Many authors have tried to classify pseudobulges using only one criterion; e.g., (1) that $n < 2$ or (2) that they deviate from the Kormendy (1978) correlation between r_e and μ_e, usually toward low surface brightness. However, almost all of the half-dozen or so classification criteria listed in the above references have at least a few exceptions. So it is safest to base classifications on more than one criterion. Here, the first sign of a pseudobulge contribution is apparent flattening; e.g., a local maximum in ellipticity ϵ in Figure 6, accompanied by a higher-surface-brightness "ring" in the brightness profile. We also use the constraint that classical bulges have $n \gtrsim 2$.

The studies that first recognized pseudobulges and that established the secular evolution paradigm concentrate on extreme examples—galaxies that contain essentially only a pseudobulge and a disk as contrasted with galaxies that contain only a classical bulge and a disk. But these studies recognize that galaxies can and often do contain both a classical bulge and a pseudobulge. A few attempts to disentangle these components have been made (e.g., Erwin et al. 2015, and references therein). NGC 4826 proves to be such a galaxy. Moreover, the pseudobulge in NGC 4826 is complicated: it consists of two distinct disks or rings with steep outer cutoffs ($n \ll 0.5$) plus a more diffuse part. The rings are easy to model definitively. But the diffuse part of the pseudobulge necessarily is difficult to distinguish from the classical bulge. Our photometric decomposition therefore has coupled uncertainty between the classical bulge and part of the pseudobulge. For this reason, we show two "error bar" decompositions constrained by the known properties of pure classical bulges and pure pseudobulges. These uncertainties affect only Section 5.2, the comparison of our derived black hole mass with bulge and pseudobulge total luminosity. They do not affect our machinery to measure black hole mass.

We emphasize that our decomposition of the brightness distribution of NGC 4826 into multiple classical bulge, pseudobulge, and disk components is analogous to multi-Gaussian decompositions as used in black hole mass measurements (e.g., Monnet et al. 1992; Emsellem et al. 1994; Verolme et al. 2002; Cappellari et al. 2002). For purposes of mass measurement, it is not necessary to attach physical interpretation to the components with which the stellar density distribution is modeled. It is necessary only that the model reproduces the observed density distribution accurately. In our case, bulge–pseudobulge–disk decomposition using Sérsic functions allows us to do this accurately (Figure 6) with fewer components than would be required with multi-Gaussian expansion. But interpretation of the components—which never is relevant for multi-Gaussian expansion—is relevant here only in Section 5.

Anticipating Section 5, we return to formation processes. A large body of work has produced a new paradigm of the slow ("secular") evolution of disk galaxies that complements our picture of galaxy evolution by hierarchical clustering and galaxy mergers. Quoting Kormendy (2015), "Secular evolution happens because self-gravitating systems evolve toward the most tightly bound configuration that is reachable by the evolution processes that are available to them. They do this by spreading—the inner parts shrink while the outer parts expand. Significant changes happen only if some process efficiently transports energy or angular momentum outward." Common driving agents are galaxy bars and oval disk distortions. Morphological features of galaxies such as nuclear, inner, and outer rings are now understood to be products of this secular evolution. Pseudobulges appear to be a natural consequence of this evolution. Observational and theoretical galaxy evolution work have proceeded in parallel and have illuminated each other. However, the existence of the above morphological features was revealed observationally before they were understood to be part of the secular evolution picture. Secular evolution and its relation to galaxy morphology is reviewed from an observational perspective by Kormendy (1993b, 2013, 2016) and Kormendy & Kennicutt (2004), and from a theoretical perspective by Tremaine (1989) and Sellwood (2014). Conferences that concentrate on secular evolution include Special Session 3 on "Galaxy evolution through secular processes" at the 2012 IAU General Assembly (see Kormendy 2015) and the 2011 Canary Islands Winter School on Secular Evolution (see Kormendy 2016). Thus substantial literature establishes the physical basis for why and how pseudobulges form. These results have proved to be useful in a variety of contexts. For example, (1) every letter in a complicated galaxy classification such as (R)SB(r)b (de Vaucouleurs et al. 1991)—where (R) means "outer ring" and (r) means "inner ring"—is now understood at least heuristically within the complementary paradigms of hierarchical clustering and secular galaxy evolution. Also (2) correlations of bulge-like components with the masses of supermassive black holes

are different for classical bulges and pseudobulges: Classical bulges correlate tightly with black hole mass, whereas pseudobulges show little or no correlation with black hole mass (see Kormendy & Ho 2013a for a review and Section 5.2 for NGC 4826 as an example).

We conclude this section with an important comment: Although we identify and model the pseudobulge of NGC 4826 in the way that is done for galaxies that underwent secular evolution—that is, we define as a pseudobulge the inner parts of the galaxy that are diskier than the classical bulge—we will conclude that NGC 4826's "pseudobulge" was manufactured via a cold-gas accretion and not by evolution that was driven by a bar or oval. To our knowledge, NGC 4826 is unique. Its unusual evolution plausibly has been driven by gas that was accreted counter-rotating with respect to gas already in the galaxy. The latter was evidently more important, because the gas in the dust disk corotates with the stars. But interaction between corotating and counter-rotating gas will have reduced the net angular momentum and dumped an unusual amount of gas—some of which formed the pseudobulge—near the center. This is thought to be the reason for the unusually prominent dust disk.

2. Imaging and Photometry

Figures 1 and 2 show color composite images of the galaxy. Figure 1 is the iconic HST Hubble Heritage picture of the well known dust disk. Figure 2 shows, surprisingly, that the region that is strongly absorbed in Figure 1 is actually a bright "shelf" in the less-obscured infrared surface brightness and hence in stellar density. This is classically called a "lens" component, although here it is more likely to be a result of star formation in accreted gas rather than a product of the different formation mechanism that makes lens components in barred galaxies (Kormendy 2013). Figure 2 emphasizes the lens component and the fact that the dusty lens region is only a small central part of a galaxy whose dominant disk extends to much larger radii.

2.1. *Near-infrared* K_s *Composite Profile Corrected for Internal Absorption*

We need to measure the near-infrared surface brightness profile corrected for internal absorption. Unlike the absorption in visible light (Figure 1), the absorption at K_s is small enough to be correctable, and the absorption at longer wavelengths $>3\,\mu$m is assumed to be negligible. This section provides nonparametric measures of surface brightness, ellipticity, and position angle (PA) that are used for the stellar mass distribution in the dynamical modeling. Separate from this nonparametric use, this profile is used in Section 2.3 to estimate the bulge, pseudobulge, and disk contributions of the galaxy. We need to understand these components in order to interpret a black hole mass (M) measurement or upper limit in the context of observed correlations between M and host galaxy component properties.

The K_s-band image that provides surface brightnesses and the zero-point used in this paper comes from the 2MASS Large Galaxy Atlas (Jarrett et al. 2003) via the NASA/IPAC Infrared Science Archive.[10] The effective wavelength is 2.2 μm and the scale is $0\farcs10$ pixel^{-1}. Foreground stars were cleaned by interpolation using a plane fitted to a square annular region surrounding the star. We were careful to exclude the PSF wings. The image was unsmoothed at small radii and Gaussian smoothed with FWHM = 3 pixels at $76''$–$165''$ and FWHM = 7 pixels at larger radii. Care was taken to ensure that smoothing does not degrade the profile. Profiles were measured by JK using the Lauer (1985) surface photometry package in the Lick Observatory image processing system XVISTA (Stover 1988). All photometry discussed in this section was carried out as above.

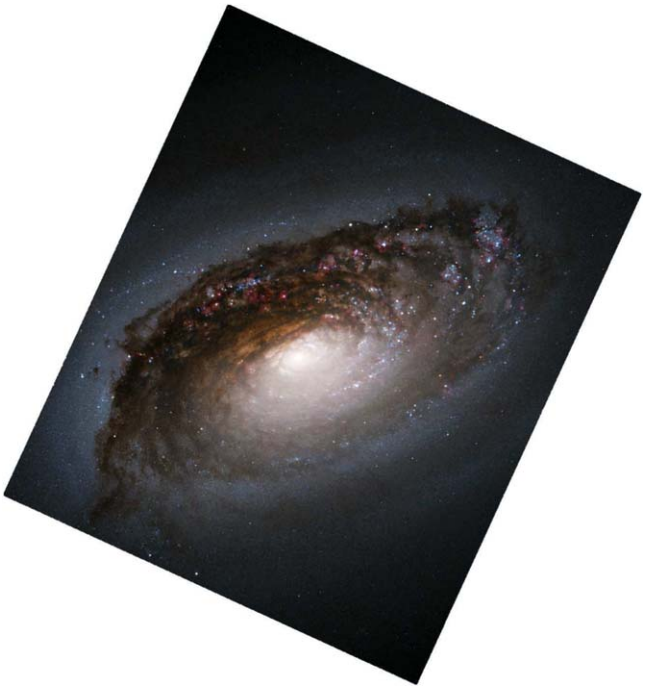

Figure 1. Multiband image of NGC 4826 from STScI's Hubble Heritage project. HST data used to make the image come from two programs: GO-8591 and GO-9042. Colors are blue: F450W (B), cyan: F547M (Strömgren y), red: F656N (Hα), and pink: F814W (I). North is up; east is left, and the NE side of the galaxy is the nearside. The long axis of the rectangular bounding box is $137''$. The prominent dust lanes, a clear view of the small bulge, and inclination angle of the disk are evident from the image. At small radii, there is a composite classical bulge plus pseudobulge (Kormendy & Kennicutt 2004; Kormendy 2013; Kormendy & Ho 2013a). Decoupling these components is necessary to interpret correlations between black hole mass and bulge properties. Parameters of two overlapping components are strongly coupled even in the absence of dust, and deriving them here required special care. A key revelation from our analysis is that the internally absorbed and very dark parts of the inner galaxy (in this figure) are actually higher in stellar density than the outer disk (Figure 2). To understand NGC 4826, we need photometry that is as absorption-corrected as possible.

In the K_s band, the dust disk is much less prominent than in the visible, but internal absorption remains significant. We therefore corrected the region of the dust disk and smaller radii using the 2MASS J-band image and the procedure described in Nowak et al. (2008) and Bender et al. (2015). Rephrasing the discussion from the latter paper for the present bandpasses, let f_J and f_{Ks} be the J- and K_s-band surface brightness fluxes per square arcsecond, respectively. A subscript "0" refers to an extinction-corrected quantity, and the lack of it indicates magnitudes or fluxes as observed. From the relation,

$$A_{Ks} \equiv K_s - K_{s,0} = \alpha E(J - K_s), \tag{1}$$

where A_{Ks} is the K_s-band absorption and $E(J-K_s) \equiv (J-K_s) - (J-K_s)_0$ is the reddening in the color $(J-K_s)$,

[10] https://irsa.ipac.caltech.edu/frontpage

Figure 2. Multicolor color composite images of NGC 4826. The left image is a *gri*-band composite from the Sloan Digital Sky Survey via NED. The right image is a color composite made using the sum of 2MASS *J*, *H*, and *K* images for the blue channel, the Spitzer Space Telescope Channel 1 image at 3.55 μm for red and the average of the two for green. Both panels show the same field of view, the width of which is $11\farcm9$; north is up and east is left. The right panel shows the Figure 1 HST Hubble Heritage field outlined in black. The dusty disk that dominates visible bandpasses is a slightly rim-brightened bright disk (a "lens"component) when seen in the infrared, where dust extinction is less important.

it follows that:

$$f_{Ks,0} = \frac{f_{Ks}^{\alpha+1}}{f_J^{\alpha}} \frac{f_{J,0}^{\alpha}}{f_{Ks,0}^{\alpha}}. \quad (2)$$

We assume that the stellar population gradient in the inner part of NGC 4826 is negligible, because we see little color gradient between observed *H* and *K* profiles and between (see below) dust-corrected K_s-band and observed 3.368 μm- and 3.55 μm-band profiles. Then $f_{J,0}/f_{Ks,0}$ is approximately constant and so:

$$f_{Ks,0} \propto \frac{f_{Ks}^{\alpha+1}}{f_J^{\alpha}}, \quad (3)$$

where

$$\alpha = (A_J/A_{Ks} - 1)^{-1} \approx 0.62. \quad (4)$$

Here we adopt the mean of the standard extinction curves in Finkbeiner et al. (1998) and in Mathis (2000). The correction is not perfect: it is based on the assumption that all of the dust is in a screen in front of the image, whereas here, most of the dust is expected to be in the galaxy disk plane. However, the correction works well, as evidenced by the observation that the $\mu_{Ks,0}$ profile generated as above agrees with the profiles derived below in bandpasses with effective wavelengths >3 μm. In particular, the above extinction profiles give, in comparison to *V* band, $A_{Ks}/A_V \simeq 0.11$, $A_{\rm WISE}/A_V = 0.051$ (WISE observatory Band 1 at 3.368 μm), and $A_{\rm Spitzer}/A_V = 0.050$ (Spitzer Space Telescope IRAC Channel 1 at 3.55 μm). We neglect internal absorption in the latter two bandpasses.

The central part of the adopted K_s-band composite profile was measured using two images from HST GO program 9360 (R. Kennicutt, PI) and downloaded from the Hubble Legacy Archive.[11] Both were taken with the NICMOS NIC3 camera; the scale is $0\farcs10$ pixel^{-1}, and the filters used are F160W and F190N. We tried to dust-correct the F190N image using the F160W image, but the bandpasses are too similar and the procedure failed. Noting that the maximum dust correction of the 2MASS K_s-band image was only about 0.1 mag arcsec^{-2}, we assume that we get a good approximation to the absorption-free near-infrared brightness profile of NGC 4826 by zero-pointing the uncorrected F160W and F190N profiles to the dust-corrected 2MASS profile where they overlap and where the resolution of 2MASS is still good enough. The HST profiles were zero-pointed to 2MASS in this overlap region, $7'' \lesssim r \lesssim 28''$, where *r* is major-axis radius.

We get two important benefits from adding profile measurements from further into the infrared at effective wavelengths 3.368 μm from the WISE observatory (Wright et al. 2010) Band 1 and 3.55 μm from the Spitzer Space Telescope (Werner et al. 2004) IRAC (Fazio et al. 2004) Channel 1, both downloaded from NASA/IPAC. First, the Spitzer images have spatial resolution FWHM $\approx 1\farcs66$ and (resampled) scale $0\farcs75$ pixel^{-1} almost as good as that of 2MASS, but they are much deeper and they have very constant sky brightnesses. Thus we can measure the profile much farther out in the galaxy with Spitzer than with 2MASS. At wavelengths longer than 3 μm, the internal absorption is also so small that it is effectively negligible. Agreement between the Spitzer + WISE profiles and the dust-corrected (but not the dust-uncorrected) 2MASS profile gives us confidence that we have removed the effects of the dust disk as well as possible. The WISE image has scale $1\farcs375$ pixel^{-1}, but the resolution is $\sim 6''$. It is therefore useful only in the region of the dust disk, where it confirms the conclusions from 2MASS and from Spitzer that what looks so faint in the optical is really a high-surface-brightness disk component. At $r < 16\farcs5$, the resolution of WISE is too poor to be useful, and at $r > 266''$, the galaxy surface brightness gets faint enough that confusion of star images with each other becomes too serious to be corrected. However, at intermediate radii, the agreement between the Spitzer and WISE profiles increases our confidence in the composite profile. The Spitzer and WISE profiles are zero-pointed to the dust-corrected 2MASS K_s profile.

[11] See http://hla.stsci.edu/hlaview.html.

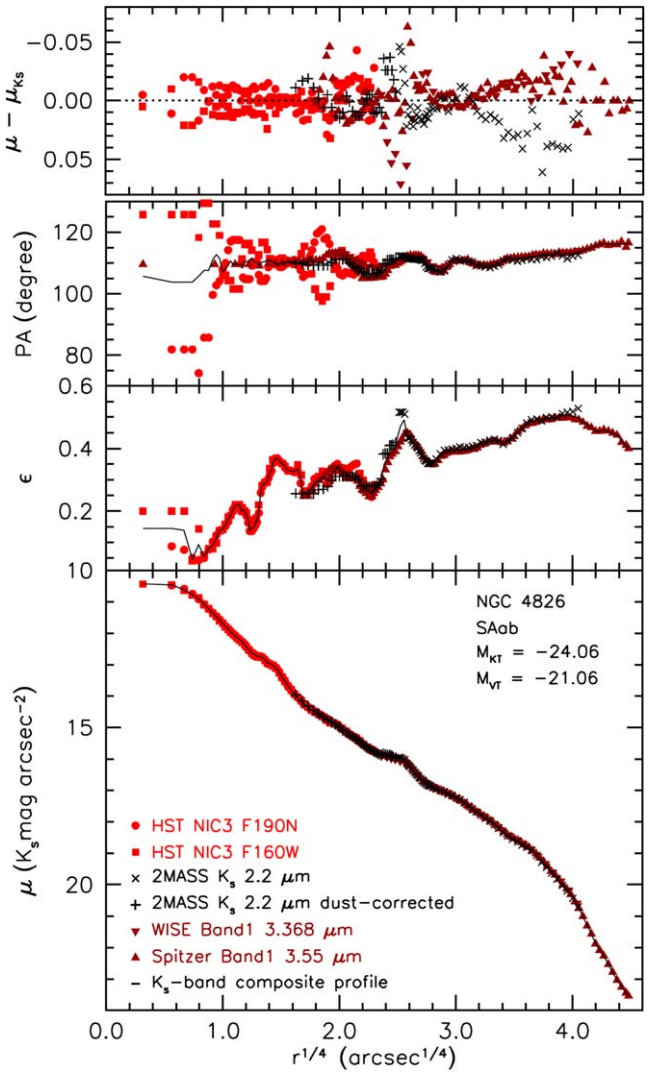

Figure 3. Composite surface photometry of NGC 4826 in K_s and redder color bandpasses. The K_s-band zero-point is on the 2MASS photometric system (Cutri et al. 2003; Jarrett et al. 2000). Outside the radii of the dust disk, the 2MASS K_s image was measured without absorption corrections; it provides the zero-point. Within the dust disk, the K_s image was corrected for internal absorption as described in the text. The HST NICMOS NIC3 profiles were then shifted to this absorption-corrected profile. At large radii, 3.368 μm WISE and 3.55 μm Spitzer Space Telescope profiles were shifted to the 2MASS K_s profile. The four panels show (bottom to top) major-axis surface brightness, ellipticity, major-axis position angle PA east of north, and (given that the scatter is too small to see in the bottom panel) departures of the individual profiles from the mean K_s composite profile shown in the bottom panel by the solid black curve. It is important to note that the top panel shows that color gradients between K_s and >3 μm are small. Here and elsewhere, photometric profiles are plotted against $r^{1/4}$ so that Sérsic $n < 4$ profiles (concave down) are easily distinguished from $n > 4$ profiles (concave up). We do not plot μ against $\log r$, because no components have $\mu \propto \log r$.

All the above profiles are overplotted in Figure 3. Only the data that were averaged are shown. We pruned out points at small radii that are affected by spatial resolution that is poorer than that of HST. We also pruned out points at large radii that are affected by nonuniform sky brightness or by overlapping star PSFs. The mean composite profile shown in Figure 3 by a black solid curve is used in Section 2.3 to decompose the galaxy profile into classical bulge, disky pseudobulge, and outer disk components.

In the bottom panel of Figure 3, deviations between the different telescope and bandpass measurements are too small to be visible. We therefore add a top panel which shows their deviations from the mean composite profile with an expanded magnitude scale. The important things to note here are (i) that the Spitzer and WISE profiles agree with the dust-corrected 2MASS K_s profile—this provides reassurance about the profile measurements and dust correction—and (ii) that there is evidence for only a small color gradient, at least at these infrared wavelengths. This justifies our assumption in Equation (3) that the stellar population gradient is sufficiently small that we can assume that $f_{J,0}/f_{K,0}$ is approximately constant.

Integrating the composite surface brightness and ellipticity profiles gives a total magnitude of $K_{s,0} = 5.256$, where the subscript "0" indicates that the magnitude is corrected for internal but not Galactic absorption. The 2MASS Large Galaxy Atlas gives an integrated apparent magnitude of 5.330. Given that 2MASS does not correct for internal absorption, this is excellent agreement.

We adopt $(V - K_s)_0 = 3.00$ from Kormendy & Ho (2013b). Then the absolute magnitudes of the galaxy are $M_{K,s} = -24.06$ and $M_V = -21.06$. Component magnitudes are derived in Section 2.3.

2.2. High-resolution Central Imaging and Stellar Dynamical Model

To look for a supermassive black hole in NGC 4826, we need to construct dynamical models that have spatial resolution much higher than those of either the photometry or the kinematic measurements. Then models are constrained to fit the observations after PSF convolution. This means that we need a surface photometry model that is much higher in spatial resolution than the K_s-band photometry achieved in Section 2.1 with the HST NIC3 PSF and $0\farcs10$ pixels.

We used the STIS acquisition image to create a light model at the smallest scales. STIS has a spatial scale of $0\farcs0508\,\mathrm{pixel}^{-1}$. Figure 4 shows the resulting profile zero-pointed to K_s. Also shown is the adopted light profile at perfect spatial resolution (as used in the dynamical models) and after convolution with a Gaussian PSF with FWHM $= 0\farcs13$. The unconvolved model surface brightness (black line) is able to match both the STIS and NIC3 data when convolved and sampled with the appropriate PSF and pixel scale. Thus we are confident in the consistency of our multiband photometry and ability to model the light distribution at small scales.

2.3. Photometric Decomposition

Masses M of supermassive black holes are observed to correlate with the luminosities, stellar masses, and stellar velocity dispersions of elliptical galaxies and of classical bulges of disk galaxies but not with galaxy disks, not with pseudobulges, and (apart from implications of the correlations with ellipticals) not with dark matter halos (see Kormendy & Ho 2013a for a review). Therefore, to interpret the mass of any black hole that we detect in NGC 4826, we need to understand the structural components of the galaxy. This requires photometric decomposition, and we use this decomposition as the basis of our surface-brightness deprojection to luminosity density, which is necessary for our kinematic modeling. We adopt the photometric decomposition shown in Figures 5 and 6.

Our understanding of the photometric decomposition possibilities in NGC 4826 is guided by previous studies of disk-dominated galaxies. For reviews on classical bulges and

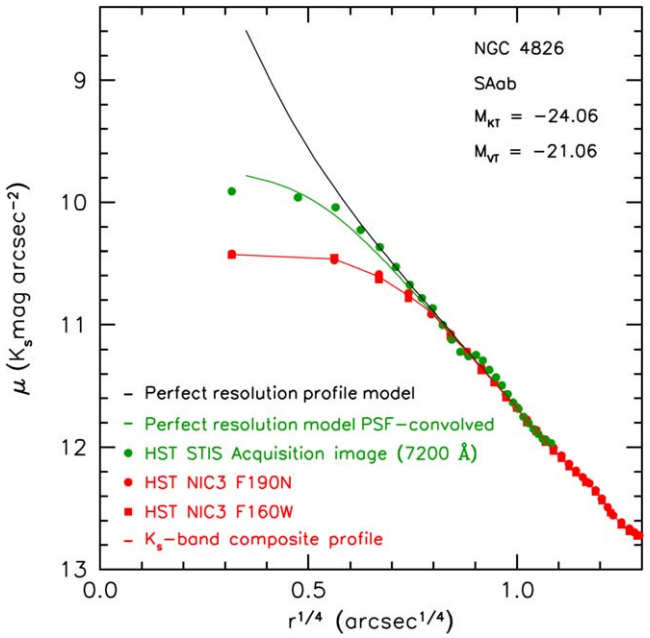

Figure 4. Photometric model of the stellar light distribution at small spatial scales used in dynamical modeling. The NICMOS NIC3 profiles and the inner part of the K_s-band composite profile from Figure 3 are shown in red. A profile measurement of the ∼7200 Å STIS acquisition image is shown with green points, zero-pointed to K_s. The adopted perfect-resolution light profile used near the center of the galaxy is shown in black and (after PSF convolution) by the green curve. At radii larger than those shown here, the K_s-band composite profile (including ellipticities) was used to model the stellar light distribution.

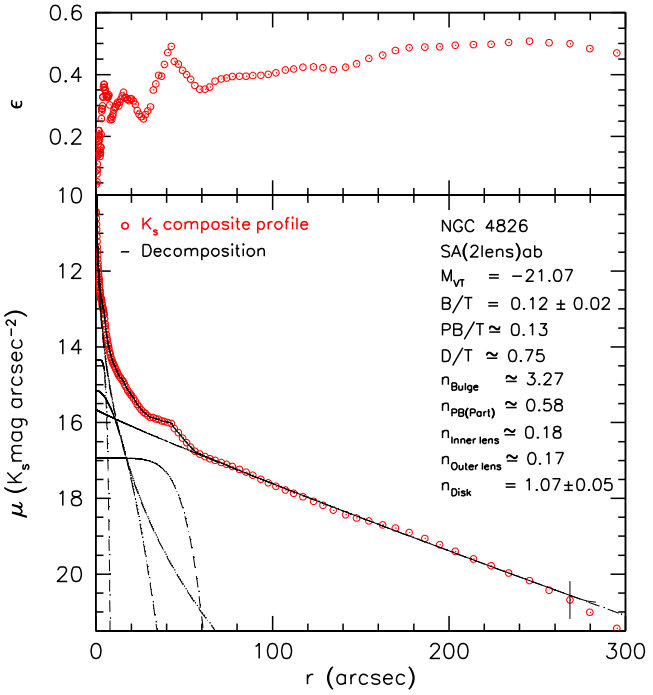

Figure 5. Adopted photometric decomposition of the composite K_s-band surface brightness profile of NGC 4826 here plotted against major-axis radius r to emphasize that the galaxy is dominated in radius by its exponential disk. The lens component revealed in Figure 2 is the prominent "shelf" in surface brightness with outer radius ∼45″. A Sérsic (1968) profile fit to this is shown by the outer dashed profile; it has index $n_{\rm Outer\ lens} \simeq 0.17$ (with K-band surface brightness $\mu_{eK} = 16.75$ at effective radius $r_{eK} = 23\farcs0$). The inner components are, from the outside inward at 20 mag arcsec^{-2}, the outer lens, a classical bulge with $n_{\rm Bulge} = 3.27$ ($\mu_{eK} = 14.98$; $r_{eK} = 7\farcs4$), the rest of the pseudobulge fitted with a Sérsic function with $n_{\rm PB(Part)} = 0.58$ ($\mu_{eK} = 15.96$; $r_{eK} = 11\farcs3$), and an inner lens with $n_{\rm Inner\ lens} = 0.18$ ($\mu_{eK} = 14.38$; $r_{eK} = 3\farcs1$). The disk is approximately exponential ($n = 1.07$ with K-band surface brightness $\mu_{eK} = 17.64$ at effective radius $r_{eK} = 101\farcs1$). The inner components are better seen in Figure 6, which plots surface brightness against $r^{1/4}$. The three parts of the pseudobulge (the outer lens, the rest of the pseudobulge [PB(Part)], and the inner lens) add up to have $PB/T \simeq 0.13$, almost the same as the classical-bulge-to-total luminosity ratio $B/T \simeq 0.12 \pm 0.02$. The sum of the components shown by dashed curves is represented by the solid curve. The decomposition fit is made between the vertical dashes across the profile points (the inner one is at $0\farcs4$).

ellipticals, see Kormendy et al. (2009) and Kormendy & Bender (2012), and for reviews of disk secular evolution and pseudobulges, see Kormendy (1993b, 2013, 2016) and Kormendy & Kennicutt (2004). Classical bulges and elliptical galaxies are essentially indistinguishable in their structure and structural parameter correlations. At $M_V > -21.6$, they have Sérsic indices $n < 4$; in fact, usually $n \simeq 1.8$–3 for small bulges like the one in NGC 4826. Except near the center (a few percent of the total light), classical bulges are well described by single Sérsic functions with slowly variable flattening, such that significant departures that are localized in radius or azimuth deserve interpretation. The kind of pseudobulge that is relevant here—"disky pseudobulge"—is more disk-like than are classical bulges. They are flatter (often as flat as the outer disk); and, in galaxies with overall star formation (not S0s), they generally contain disk gas and star formation. They often have smaller velocity dispersions than classical bulges. A relevant observation for NGC 4826 is that the velocity dispersion decreases toward the center (see NGC 1553, whose pseudobulge has a smaller velocity dispersion than its surrounding disky lens component; Kormendy 1984). Disky pseudobulges are thought to form via star formation in gas that is driven toward galaxy centers by disk secular evolution—by gradual rearrangement of the angular momentum distribution driven by galaxy bars, global oval distortions, and perhaps other global asymmetries (see the above reviews). One reason for this idea is the strong association of pseuduobulge classification features with the presence of such asymmetries.

In this context, it is important to emphasize that NGC 4826 shows no signs of any structural azimuthal asymmetries that are expected to drive secular evolution. This does not guarantee that such features did not exist in the past and have evolved away. Bars destroy themselves if they increase the central mass concentration in a galaxy (see Kormendy 2013 for a review), e.g., via the abovementioned secular evolution. NGC 1553 is an example of a galaxy that now has a lens but no bar or discernible oval; the lens component may have been a bar in the past (Kormendy 1979, 1984, 2013). We expect that lenses made via the azimuthal phase-mixing of elongated "x_1" bar orbits should have large radial velocity dispersions, and the lens of NGC 1553 has a large radial velocity dispersion (Kormendy 1984). The outer lens-like disk in NGC 4826, however, is cold. There is strong evidence that NGC 4826 has accreted gas-rich small galaxies: the outer gas disk counter-rotates with respect to the inner galaxy. We see strong evidence for a pseudobulge contribution in NGC 4826. This suggests that lens components specifically and disky pseudobulges more generally can be formed in another way that does not involve bar-driven secular evolution. That is, pseudobulges can also form via gas accretion followed by star formation. Lenses formed this way are expected to be recognizable via their small velocity dispersions. NGC 4826 proves to contain such a pseudobulge including two lens components. The cause of the

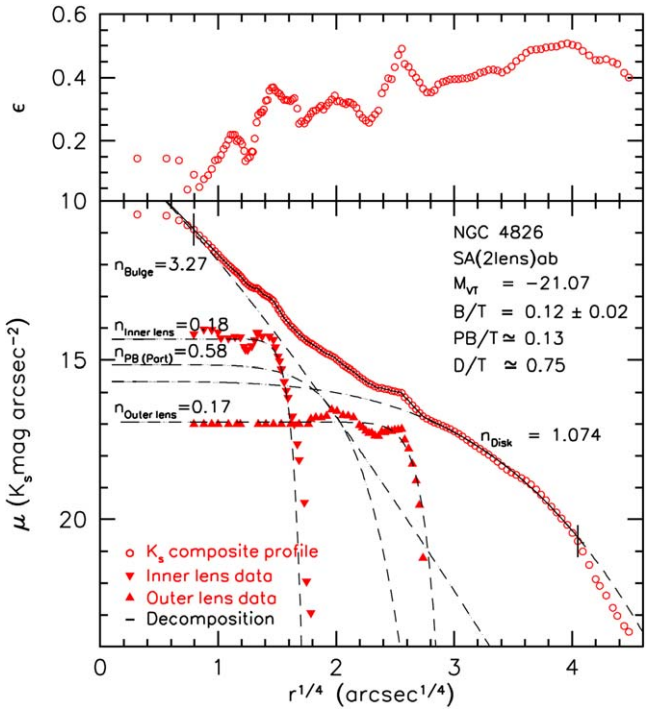

Figure 6. Adopted photometric decomposition plotted against $(r/\mathrm{arcsec})^{1/4}$ to show components at both small and large radii. The lens component shown in Figure 2 proves to be the outer of two "shelves" in surface brightness; these lens components have almost the same, very small Sérsic index. In practice, we use their profiles as the data points that remain when the rest of the model is subtracted from the composite profile. Both sets of lens data points are chosen to have constant surface brightness inside the radial range where they are well measured by the composite profile and decomposition model (that is, we interpret these as lens components, not as rings that are dark inside). When the two lenses and the outer disk are subtracted from the composite profile, the rest of the galaxy is well fitted by two Sérsic functions, an inner one with $n_{\mathrm{Bulge}} \simeq 3.27$ that we identify as the classical bulge and an outer one with $n_{\mathrm{PB\,(Part)}} = 0.58$ that we consider, together with the two lens components, to be the pseudobulge. The classical and pseudo parts of the bulge are approximately equal in importance in this favored decomposition. See the Appendix and the discussion in Section 2.3 for alternative decompositions. Again, the sum of the components shown by the dashed curves is represented by the solid curve, and the fits are made between the vertical dashes across the profile points.

unusual structure of NGC 4826 plausibly is the recent accretion of gas that now counter-rotates with respect to the galaxy at large radii. Collision of arriving, counter-rotating gas with corotating gas then still at large radii is expected to drive large amounts of gas toward the center (e.g., Rubin 1994; Rix et al. 1995).

Many galaxies are observed to contain only a classical bulge (e.g., M81) or only a pseudobulge (e.g., NGC 4736). It is also true—and less well studied, because decomposition is tricky—that many galaxies contain both components (e.g., Erwin et al. 2003; Kormendy 2013, 2016). NGC 4826 has long been considered to be in this category. The weight of conflicting evidence led Kormendy (1993b), Kormendy et al. (2011), and Kormendy & Ho (2013a, 2013b) to classify the galaxy as having a pseudobulge. Here, we recognize that both a classical and a pseudobulge are present, and we try to disentangle them to properly quantify their relative contributions. Their parameters are inevitably coupled. As a result and based on experience summarized above, we derive three models, a preferred one (Figures 5 and 6) and two "error bar" models that have the smallest and largest plausible classical bulges (Appendix Figures 16 and 17). The error bar models are disfavored but not robustly disproved. Conclusions about black hole correlations are more robust if they are relatively independent of the decompositions on which they rely.

Note from the ellipticity profiles in Figures 5 and 6 that the outer lens component is, at its rim, as flat as the flattest part of the outer disk. Even the inner bump in the profile at $(r/\mathrm{arcsec})^{1/4} \simeq 1.5$ is flatter than the surrounding (pseudo) bulge—it, too, is a disky "inner lens" component. Also note that the (pseudo)bulge is flatter between the two lens components than it is interior to the inner lens component—it is not much thicker vertically than the thickest parts of the outer disk. We conclude that a disky pseudobulge contributes more importantly in this radial range $(r/\mathrm{arcsec})^{1/4} \simeq 2$ than it does near the center. Although the observation that σ decreases toward the center in the STIS spectroscopy leads us to suspect that some pseudobulge light contributes here, too. It is worthwhile to keep this in mind, but we do not include it in the decomposition.

The preferred decomposition shown in Figures 5 and 6 was derived iteratively, as follows.

A first decomposition was made between 30″ and 260″, i.e., the radial ranges where the disk is exponential and, nearer the center, where the outer lens dominates the light. The disk was constrained to be nearly exponential; the Sérsic index of the lens—which included a contribution from the (pseudo)bulge—was a free parameter. The decomposition program converged to $n_{\mathrm{Disk}} = 1.07 \pm 0.05$ and $n_{\mathrm{Outer\ lens}} = 0.17 \pm 0.03$.

The above two fitted models were then subtracted from the composite profile and a decomposition was run with a Sérsic function fitted to the small bump in the profile at $(r/\mathrm{arcsec})^{1/4} \simeq 1.5$ (radius $\simeq$5″) and another Sérsic function fitted to the rest of the profile. This gave a fit to what proves to be a tiny inner lens with $n_{\mathrm{Inner\ lens}} = 0.18 \pm 0.03$. This fit is shown by a dashed line labeled with the Sérsic index in Figure 6, but at the end, it was replaced with the data points shown by the upside-down filled triangles, i.e., the composite profile minus the sum of the rest of the model fits (classical bulge plus pseudobulge plus outer lens plus disk). Similarly, the outer lens fit is shown by a dashed curve labeled with the Sérsic index, but in the end, it was replaced with the filled triangles, i.e., the composite profile minus the rest of the decomposition model.

Finally, a profile was constructed from the K_s-band composite that should include only the classical bulge and the part of the pseudobulge that is not the inner or outer lens. This profile was decomposed into two Sérsic components that are shown in Figures 5 and 6. The index of the classical bulge, $n_{\mathrm{Bulge}} \simeq 3.27$ is a little larger than expected but is reasonable for a small bulge. We have no expectations regarding the index of the rest of the pseudobulge; the decomposer chose $n_{\mathrm{PB(Part)}} \simeq 0.58$. Then the classical bulge is 12% ± 2% of the light of the galaxy, where the error bar reflects only the uncertainty in flattening, not any uncertainties about whether this decomposition is preferred compared to the other two. The sum of "PB(Part)" and the two lens components is 13% of the light of the galaxy; this agrees comfortably with the conclusion of earlier work (summarized in Kormendy et al. 2010 and Kormendy & Ho 2013a) that classical and pseudo components are roughly equally important in this galaxy. As noted above (e.g., in the context of the centrally decreasing σ), if we have erred, it is most likely that we have underestimated the contribution of the pseudobulge and overestimated the contribution of the classical bulge.

Note that, despite the Sab classification, the galaxy robustly consists mostly of a disk. We find that the exponential outer disk has $D/T \simeq 0.75$ in this decomposition. Moreover, the pseudobulge is also disky, even if its origin is different from that of the main disk. We also do not, in the above inventory, include any contribution from neutral or ionized gas; this is part of the disk, too. NGC 4826 is a field galaxy; Kormendy et al. (2010) emphasize that most giant galaxies in field environments are mostly or entirely composed of disks. They estimated $B/T \simeq 0.10$ and $PB/T \simeq 0.10$, consistent with the present, more detailed study, especially considering that, in 2010, we did not know about the outer lens and other stellar light that is absorbed at visible wavelengths by dust.

Note again the diagnostic features in Figure 6: a disk with $D/T \simeq 0.75$ dominates the total stellar light. Its flattening varies with radius, perhaps reflecting a complicated formation history. For example, the thickening at large radii may be associated with the accretion of the material that now counter-rotates in the outer galaxy. There are two well defined (albeit small: 1% and 7% of the light of the galaxy) disky lens components; they, too, are highly flattened. Classical and pseudobulges contribute roughly equally at radii between the two lenses; the galaxy is not much vertically thicker there than it is in the inner exponential disk. A classical bulge dominates only near the center, and it contains only about 12% of the stellar mass of the galaxy.

The formal uncertainties in Figures 5 and 6 and the subsequent interpretation underestimate true uncertainties in the decomposition because the assumptions that we made are not encoded in uncertainties. To get a better feel for the true uncertainties, we also constructed decompositions assuming the smallest and largest possible pseudobulges. Both were formally acceptable but at least some of their parameters would be outliers among all galaxies. Figures of these alternative decompositions are in the Appendix. Their construction is described here.

A minimal-pseudobulge model (see Appendix Figure 16) was constructed by subtracting the two lens component data points from the total composite profile and making a two-Sérsic decomposition of all the light that remains. The resulting decomposition matches the observed profile in the fit range to within a few hundredths of a mag arcsec^{-2}. The corresponding bulge-to-total ratio is $B/T = 0.30$, the disk-to-total ratio is $D/T = 0.62$, and the lenses take up the remaining 8% of the light. This decomposition is disfavored for several reasons. The disk is not exponential: The best-fit $n_{\rm Disk} = 0.87 \pm 0.04$ is smaller than $n = 1$ for an exponential. Also, the Sérsic index $n_{\rm Bulge} = 4.28 \pm 0.24$ of the classical bulge is bigger than experience leads us to expect for a small bulge. Moreover, this decomposition ignores the implication of the ellipticity profile that a pseudobulge is important at more radii than just those of the two lenses. Therefore, this decomposition is inconsistent with experience with other galaxies.

The maximal-pseudobulge decomposition (See Figure 17 in the Appendix) was made by forcing the Sérsic index of the bulge to be as small as possible. The best-fit decomposition yielded parameters $n_{\rm Bulge} = 2.45 \pm 0.20$ to optimize the fit to the observed profile. Then $B/T = 0.09 \pm 0.01$. An alternative solution is possible with $n_{\rm Bulge} = 1.93 \pm 0.19$, but it fits slightly less well, and it would imply the smallest Sérsic index that we have seen for a classical bulge. Then we would have $B/T = 0.07$. The maximal-pseudobulge fit, however, has smaller rms(μ) and is adopted as our error bar decomposition with the smallest plausible classical bulge. It has $PB/T \simeq 0.16$ and $D/T \simeq 0.75$, similar to our adopted decompositions (Figures 5 and 6).

All this may be complicated enough to be uncomfortable, but many galaxies have composite classical plus pseudobulge central components plus, in the majority of cases, disks at large radii. We need to be confident that our picture of the correlations of black holes with host galaxies is not biased by any concentration on the simplest galaxies with the fewest structural components and possibly the simplest formation histories. So we should include galaxies such as NGC 4826 in our samples. We need to be confident that our analyses—our photometric decomposition in particular here—leads to realistic results. So we need to check that the parameters of the classical bulge that we derive are realistic compared with the properties of simpler systems with purely classical bulges and ellipticals with no disk component. This is checked in Figures 18 and 19 in the Appendix. There, we see that the classical bulge of NGC 4826 is consistent with the projections of the fundamental plane structural parameter correlations. The classical bulge of NGC 4826 is among the most compact known, intermediate between M32 and more massive bulges but essentially normal.

Thus, we have a favored bulge-pseudobulge-disk decomposition and two extremal decompositions to use in our comparison of NGC 4826 with published correlations between M and host (pseudo)bulge properties. For the deprojection, we use the procedure due to Gebhardt et al. (1996). The deprojection assumes axisymmetric spheroidal geometry of the luminosity density. That is, the deprojection method assumes constant ellipticity, and the luminosity density is unique for a given inclination. Assuming that the galaxy is axisymmetric but not spheroidal, i.e., with ellipticity that varies with radius, leads to nonunique deprojections and potentially large uncertainties for nearly edge-on systems (Romanowsky & Kochanek 1997). The ellipticities for each component were considered separately. That is, the flattening of the spheroidal classical bulge was not assumed to be the same as the disky pseudobulge components. As discussed in Gebhardt et al. (2000b), the effect of incorrectly assuming spheroidal geometry will primarily lead to poorer constraints on Υ with little effect on the black hole mass estimate.

For the case of NGC 4826, we assume that the bulge and disk are coaligned so that measurement of the axis ratio of the disk (0.55) uniquely implies an inclination angle of 56°. To create our deprojected luminosity density, we use the five-component model that best describes the photometry. For the lens components, we use the Sérsic fit, which neglects the small deviations seen in, e.g., Figure 6, but these deviations are subdominant to the total surface brightness at their radii. Each component is deprojected separately and then the luminosity densities are summed for the models. For all components (disk, lenses, partial pseudobulge, and classical bulge), we assume that the mass-to-light ratio and inclination are the same. We note that our conclusions below about the mass of the central black hole are relatively insensitive to whether we include the lens and partial pseudobulges from our best-fit analysis versus our minimal- or maximal-pseudobulge model (see description above and figures in the Appendix). This is unsurprising as the lens and partial pseudobulge components are everywhere subdominant to the sum of the classical bulge and disk. Even in the maximal-pseudobulge decomposition, the sum of the

classical bulge and disk components is dominant everywhere but a small range of radii ($1.8 < (r/\mathrm{arcsec})^{1/4} < 2.0$), where the partial pseudobulge is comparable. Nevertheless, it makes sense to use the best photometric decomposition as the source of our luminosity density.

3. Spectroscopy

Our HST STIS spectra allowed us to extract kinematic information from both the gas emission lines (Section 3.1) and stellar absorption lines (Section 3.2). We only use the kinematics from the stellar absorption lines for our modeling, but the gas velocity information is interesting in its own right as well as extremely helpful for determining the kinematic center of the galaxy (Section 3.3).

3.1. Hα STIS Spectra

The STIS spectrum centered on $\lambda = 6581$ Å (Hα spectra) did not provide an independent black hole mass estimate, but it did provide useful information about the location of the black hole in the Ca II data. This is because the position of the $0\farcs1$ slit is the same for the two data sets; the centroid of the galaxy continuum falls on the same row in both.

Our reduction for the STIS Hα data began with a pipeline-processed `.flt` file. The processing includes bias subtraction, flat-fielding, and dark subtraction by the best reference dark. The two CR-split exposures were summed while rejecting cosmic rays. Remaining cosmic rays were removed without clipping emission lines. The 2D spectrum was rectified using a rotation of $-0\fdg399$. We fit our own wavelength solution from the associated `.wav` file using air wavelengths.

The kinematics of the ionized gas are shown in Figure 7. The five prominent emission lines were fit simultaneously for a common velocity and velocity dispersion. Independent line strengths were solved for, except that [N II] 6584 Å was constrained to be 2.95 times stronger than 6548 Å. Emission lines were first fit in 48 bins extending symmetrically to $\sim 5\farcs4$ from the continuum peak. The mean of these velocities provides a systemic velocity of 407.3 km s^{-1}. This agrees to 1 km s^{-1} with published radio values (de Blok et al. 2008). Next, emission lines were fit in only the inner $1''$ after an absorption template was redshifted, broadened, and subtracted using the Ca II kinematics as reference. This has the main effect of boosting the Hα line strength. The V and σ measurements were not significantly changed due to absorption correction. Finally, the green points in Figure 7 are fits using a different binning scheme where the minimum bin size is 2 pixels. We find that the kinematic trends discussed below, and asymmetric 1σ error bars, are robust.

3.2. Ca II STIS Spectra

The STIS observations of NGC 4826 were used for Ca II triplet absorption measurement. The spectrograph was operated with the G750M grating. The $52'' \times 0\farcs1$ slit was positioned at the center of the galaxy, aligned with the galaxy major axis as determined from ground-based images (PA = 110.°3). Two exposures at central wavelength 8561 Å were taken at two dither positions for a total exposure time of 4190 s, and a third exposure was taken at central wavelength 6581 Å for 2842 s. The wavelength range of the spectra targeting the Ca II absorption was 8275–8842 Å.

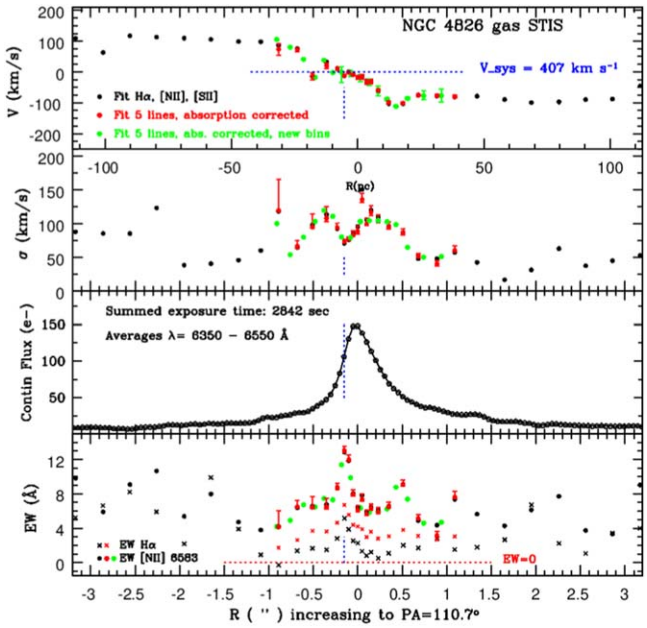

Figure 7. Kinematic parameters measured from Hα, [N II], and [S II] emission lines in STIS longslit spectroscopy. From top to bottom, we show velocity, velocity dispersion, continuum flux, and equivalent width of Hα and [N II]. A vertical dotted line marks the likely dynamical center, which is notably offset from the location of the continuum maximum.

We followed standard pipeline procedures for our STIS data reduction. First, we extracted the raw spectra from the data set and then we subtracted a value coming from a constant fit to the overscan region for bias determination. We used the Pinkney et al. (2003) iterative self-dark technique to take into account dark current as well as the warm and hot STIS CCD pixels. Next we flat-fielded, dark-subtracted, and shifted the spectra to a common dither position to combine into a final two-dimensional spectrum. One-dimensional spectra were then extracted using a bi-weight combination of rows.

3.3. Location of the Kinematic Center

The photometric center of a galaxy normally has a velocity that matches the systemic velocity, but this is not the case with NGC 4286. As we outline below, examination of both the gas emission-line profiles and the stellar absorption line dispersion profiles lead us to conclude that the kinematic center of the galaxy is offset from the photometric center, which we assume to be coincident with the peak continuum flux of the spectra. The fact that both the gas profiles and the stellar profiles agree on this point gives us greater confidence in our kinematic center determination.

The gas velocities at the continuum peak are about 19 ± 5 km s^{-1} below the systemic velocity (marked with a blue dotted line in the top panel of Figure 7). The significance of this velocity offset is bolstered by the neighboring bins. They are also below systemic and smoothly rise to 407 km s^{-1} at $R \sim -0\farcs15$, which we mark with a vertical dotted line in all panels of Figure 7. The offset of the continuum peak is likely due to a gradient in dust absorption, and the third panel of Figure 7 confirms that the continuum intensity drops off more steeply at $R < 0$ than $R > 0$. The second panel shows a dip (rather than a peak) in the gas velocity dispersion at $R \sim -0\farcs15$, but the overall gull-wing profile shows a symmetry about $R \sim -0\farcs15$. The spike in σ_{gas} at $R = 0\farcs05$

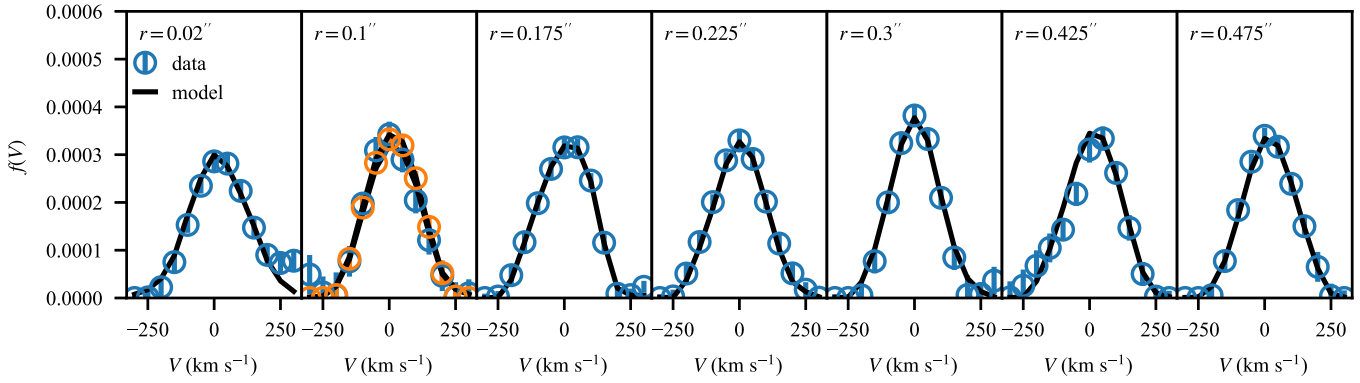

Figure 8. LOSVDs from HST/STIS observations. Each panel shows the distribution of velocities in the major-axis spatial bin indicated by the radial coordinate from kinematic center. For the $r = 0\farcs1$ bin, we plot the LOSVDs from both sides in the same panel, with the sign of velocity flipped so that they may be directly compared. The error bars indicate the 1σ uncertainties. Overall, the data show strong symmetry and high signal-to-noise, making these data good candidates for axisymmetric modeling. The best-fit model (black line) reproduces all of the major features.

disappears with rebinning and thus we ignore it. Finally, the fourth panel shows that the equivalent width of Hα and [N II] emission clearly peaks at $R \sim -0\farcs15$ and not $R = 0''$.

In the Ca II data, we find a stellar velocity dispersion peak of $132 \pm 19\,\mathrm{km\,s^{-1}}$ in the bin closest to the gas kinematic center ($R \sim -0\farcs22$). This peak is larger than all other seven bins, which range 90–100 $\mathrm{km\,s^{-1}}$. Consequently, we take this to be the kinematic center.

3.4. HET Spectra

The STIS stellar absorption line data only extend to about $1''$ before the signal-to-noise becomes low enough to make the data unuseful, and we require additional spectroscopic data in order to measure the mass-to-light ratio and the stellar orbital structure, both of which are important for a measure of the black hole mass. The large radial spectroscopic data come from van den Bosch et al. (2015), using the Marcario Low Resolution Spectrometer (Hill et al. 1998) on the Hobby–Eberly Telescope (HET). The HET spectra come from two slit positions: along the major axis and along the minor axis. The reductions follow van den Bosch et al. (2012) and van den Bosch et al. (2015). The HET spectra extend to $90''$, and allow us to calculate the slit-averaged effective velocity dispersion σ_e as

$$\sigma_e^2 = \frac{\int_0^{R_e} (\sigma^2(r) + V^2(r)) I(r) dr}{\int_0^{R_e} I(r) dr} = 104\ \mathrm{km\ s^{-1}}. \quad (5)$$

From the one-dimensional spectrum we extracted line-of-sight velocity distributions (LOSVDs) as described in Gültekin et al. (2009a), using the stellar template library due to Gebhardt et al. (2003). We experimented with several different spatial binning schemes to find the best combination of spatial resolution and signal-to-noise ratio (S/N). The best combination was a range of bin sizes from $0\farcs05$ to $0\farcs55$. We show the extracted LOSVDs in Figures 8 and 9 as well as the LOSVDs of the best-fit models from Section 4. In the second panel of Figure 8 ($r = 0\farcs1$) we have plotted LOSVDs from both sides of the galaxy, which are consistent with each other, giving us confidence that the stellar LOSVDs are not compromised by uneven dust absorption.

4. Modeling

We model NGC 4826 using the Schwarzschild (1979) orbit library method implemented by the axisymmetric three-integral code described in Gebhardt et al. (2003) and Siopis et al. (2009). Our modeling covers the classical bulge, pseudobulge components, and the region of the disk interior to radius $150''$ (5.3 kpc). NGC 4826 is sufficiently close that we did not initially fit with a dark matter halo because it is impractical to get data out to large radii where the dark matter halo density is likely to have a significant gradient. We found, however, that our modeling produced noticeably superior fits when including it. This may be a result of what could be a small mass-to-light ratio gradient at the outer portions of our spectroscopic coverage, which is well modeled by a cored logarithmic halo model with small core radius (r_c). We show the best-fit mass-to-light ratio as a function of radius in Figure 10. There is a clear preference for an increase in M/L outside of $R \approx 10''$, where the exponential disk begins to dominate the surface brightness profile (Figures 4 and 5). This is consistent with the photometric analysis of more recent star formation in the central pseudobulge than in the disk (Section 2.3). We used an iterative approach in the four-dimensional parameter space to find a global best fit and then ran a high-density grid around the best-fit location to best constrain the models. In the end, our parameter space covers $M = 0\text{–}2 \times 10^7\,M_\odot$, $\Upsilon_V = 0.3\text{–}5.25\ M_\odot L_\odot^{-1}$, $V_c = 90\text{–}190\,\mathrm{km\,s^{-1}}$, and $r_c = 0.9\text{–}2.2$ kpc. Here M is the mass of the black hole, Υ_V is the V-band mass-to-light ratio, assumed to be the same for all five photometric components, and the gravitational potential of the spherical dark halo is assumed to be

$$\Phi(r) = \frac{1}{2} V_c^2 \ln(r^2 + r_c^2), \quad (6)$$

where r_c is the potential core radius and V_c is the asymptotic velocity (Persic et al. 1996).

The modeling results that we present are based on the assumption that the black hole is located at the Ca II velocity dispersion peak of the galaxy rather than the surface brightness peak. In most galaxies, the dispersion peak and the surface brightness peak are colocated at the center of the galaxy. NGC 4826, however, has its dispersion maximum located $-0\farcs225$ from the surface brightness maximum. As described above (Section 3.1), the most likely explanation for this is that obscuration from dust is slightly higher at the true center of the

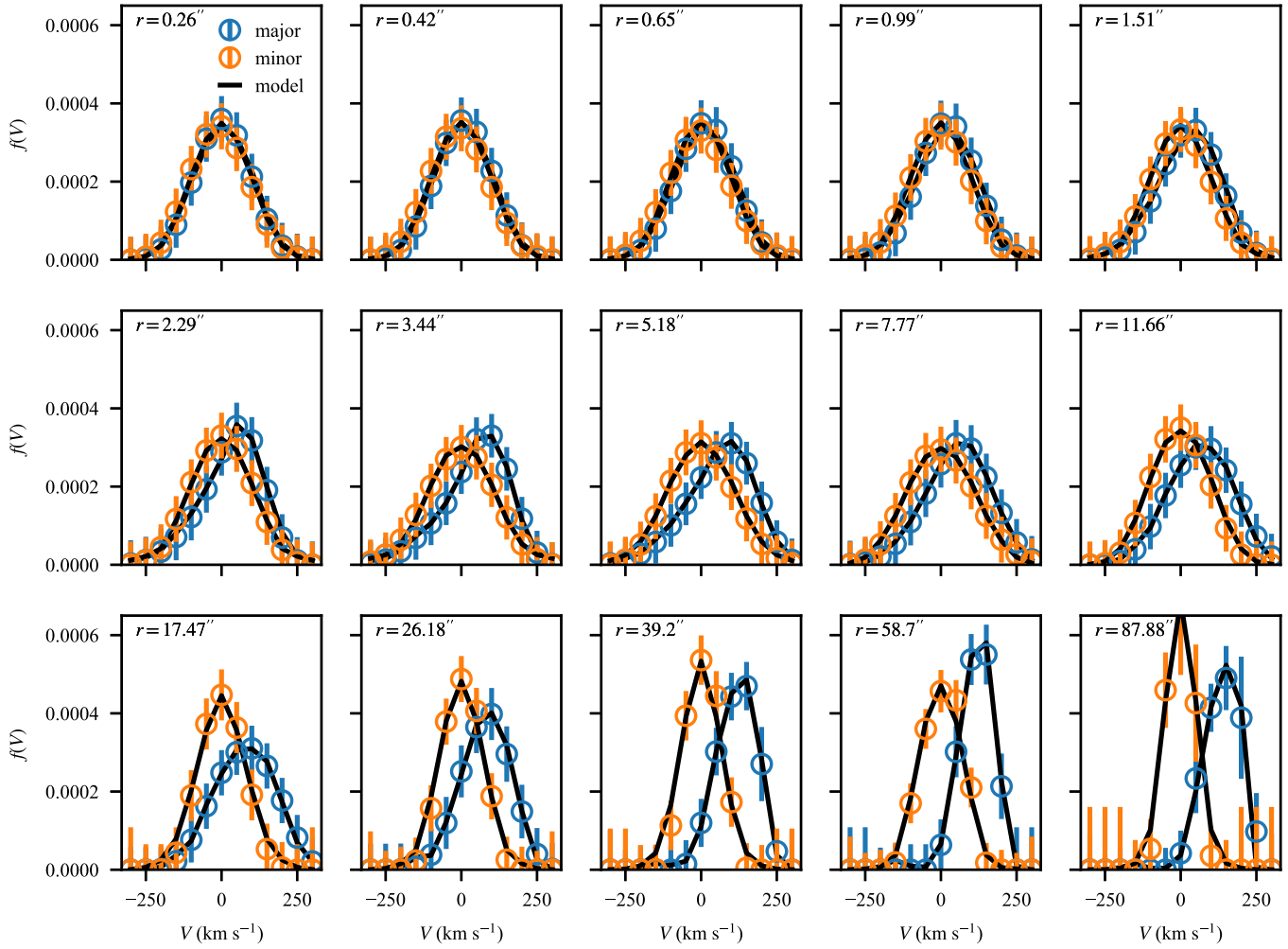

Figure 9. LOSVDs from HET observations. Each panel shows the distribution of velocities along the major (blue) and minor (orange) axes in the spatial bins indicated in each panel as distance from the kinematic center. The major-axis LOSVDs show rapid rotation in the outer parts of the galaxy, where the light is dominated by the disk, whereas the minor-axis LOSVDs are centered at $V = 0$, as would be expected in an axisymmetric system. The black line shows the best-fit model.

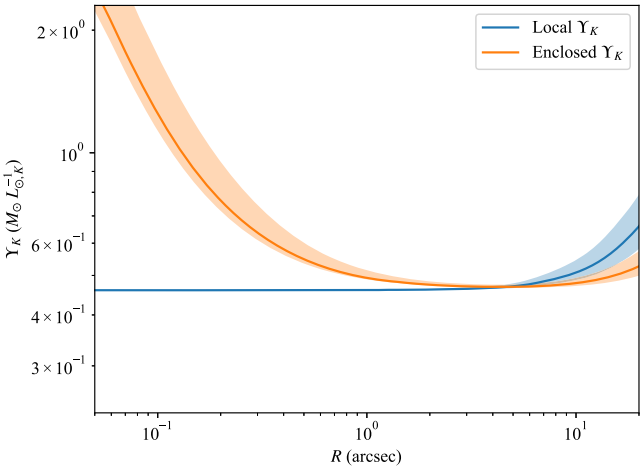

Figure 10. Mass-to-light ratio radial profiles both local (solid blue curve) and enclosed (dashed orange curve). These profiles come from the 20 models with the lowest χ^2 and show the range of plausible values. The local $\Upsilon_K(R)$ shows a flat inner portion with a slight increase starting at $R \approx 10''$. The enclosed $\Upsilon(R)$ shows the black hole dominating the total mass-to-light ratio inside of $R = 1''$.

galaxy, which is intrinsically the brightest and has the highest velocity dispersion. The fact that the gas emission-line kinematics has a slightly different location for the dispersion profile center compared to the stellar absorption lines ($-0\farcs15$ compared to $-0\farcs225$, respectively) is not significant given the different binning used. To determine the best location of the kinematic center and assumed location of the black hole, we modeled the entire system for seven locations along the STIS slit (one for each STIS spatial bin), finding that the two best were for the surface brightness maximum and velocity dispersion maximum. We further refined the location by exploring sub-bin centering at the velocity dispersion maximum because of the substantial amount of rotation seen in this spatial bin, which an axisymmetric model cannot produce if the kinematic center is in the center of the pixel. The best results were obtained when the center was assumed to be $0\farcs02$ from the center of the $0\farcs05$-wide (1 pixel) spatial bin. Because of the goodness of fit and smoothness of the rotation curve at HST resolution, we adopt this as our preferred answer.

We present the modeling results in Figure 11. Overall, the model is a good fit to the data. The results show smooth χ^2 contours with roughly parabolic shapes in individual parameters. Our best-fit parameters with 1σ uncertainties are $M = 8.4^{+1.7}_{-0.6} \times 10^6\ M_\odot$, $\Upsilon_K = 0.46 \pm 0.03$, $V_c = 168 \pm 15$ km s^{-1}, and $r_c = 1.65 \pm 0.24$ kpc. We calculate our uncertainties by taking the marginalized χ^2 curve for each parameter and linearly interpolating to a $\Delta\chi^2 = n^2$ for an $n\sigma$ uncertainty. We tried alternative estimates of

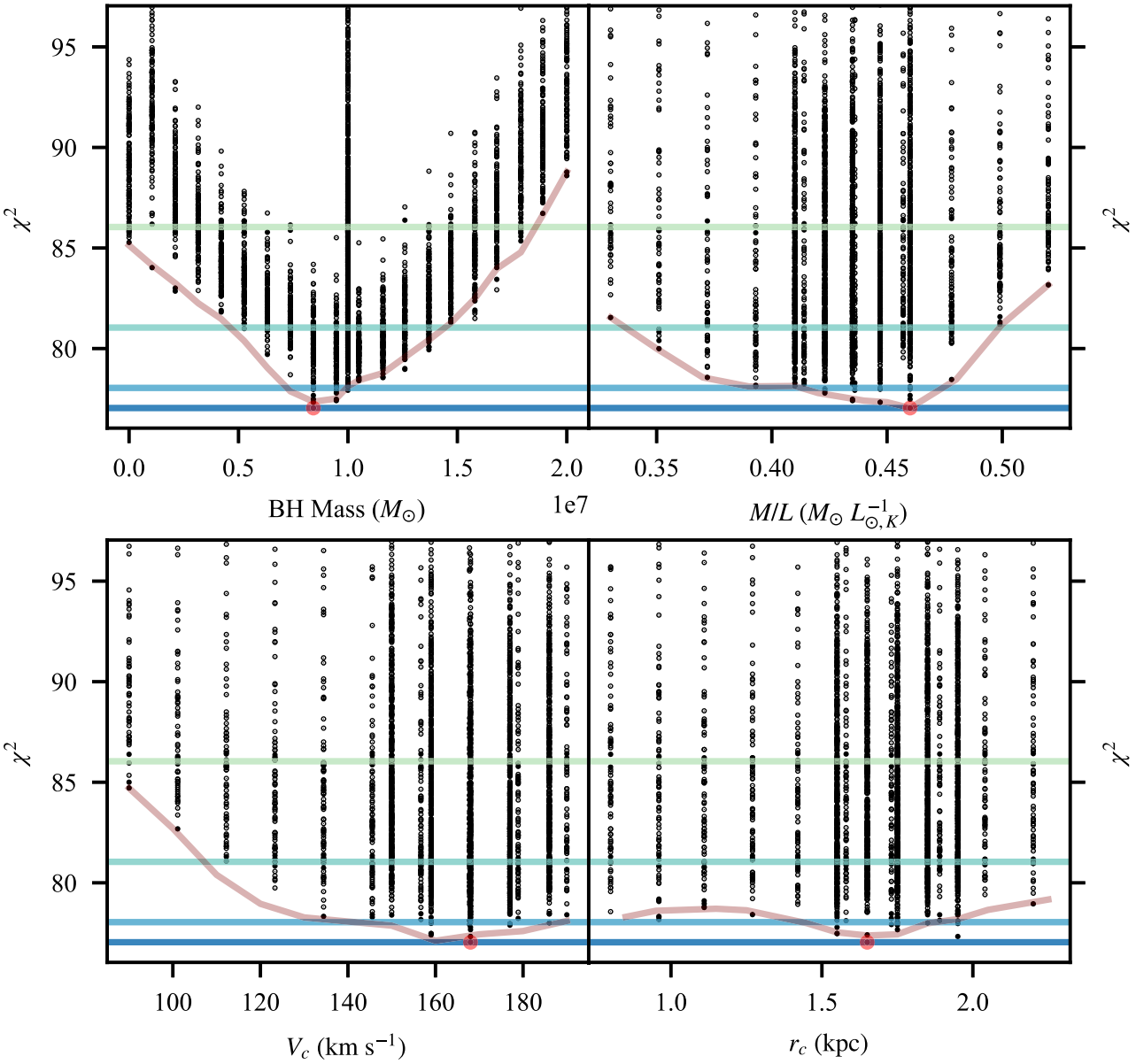

Figure 11. Modeling results. Each panel plots χ^2 against one of the model parameters (clockwise from top left: black hole mass, mass-to-light ratio, dark matter halo core radius, and dark matter halo asymptotic velocity). Each model is plotted with a black circle, and the best-fit model is plotted with a larger red circle. The purple curves are smoothed traces of the minimum χ^2 at each parameter value and show the marginalized χ^2 curve. From bottom to top, the horizontal lines show the minimum χ^2, $\chi^2_{\rm min}+1$, $\chi^2_{\rm min}+4$, $\chi^2_{\rm min}+9$ to show 1, 2, and 3σ regions for one interesting parameter. The χ^2 curves are unimodal and roughly parabolic near the minimum, indicating robust results. The best-fit mass with 1σ uncertainty is $M=8.4^{+1.7}_{-0.6}\times10^6\,M_\odot$ and is marginally consistent with $M=0$ at about the 3σ level.

the best fit and uncertainties such as fitting a parabola to the smallest χ^2 values for each value of M with a variable noise parameter. These alternative estimates resulted in similar uncertainty estimates and the minimum was usually in our 1σ interval and always in our 2σ interval. We are not able to rule out $M=0$ at 3σ as the best-fit $M=0$ model is marginally consistent at 3σ. The core radius of the dark matter halo is poorly constrained with a large range of values able to produce acceptable fits.

The velocity and velocity dispersion profiles from the best-fit models are plotted against the data in Figure 12. The internal moments of the orbits are shown in Figure 13. The anisotropy is shown as σ_r/σ_t, the ratio of the radial velocity dispersion of the stellar orbits (σ_r) to the tangential velocity dispersion (defined as the total rms tangential velocity, not merely relative to the mean rotational velocity; i.e., $\sigma_t=[0.5(\sigma^2_\phi+\sigma^2_\theta)]^{0.5}$). The anisotropy is tangentially biased almost everywhere. At large radii ($r>10''$), the tangential bias is a result of the stellar disk, which will obviously have primarily tangential motion. Inside of $r=0\farcs2$, the tangential bias may be a result of the dynamical event that produced the counter-rotating gas streams. It is worth pointing out that we do not see any evidence of counter-rotating stellar motions.

5. Discussion

The evidence for a central dark mass from our modeling raises several issues. First, is whether other data are consistent with a black hole existing in the galaxy nucleus. Second, are the implications of detecting such a low-mass black hole with Schwarzschild modeling. Third, is the matter of how such a low-mass black hole compares to predictions from scaling relations. Fourth, the relevance to LISA gravitational wave

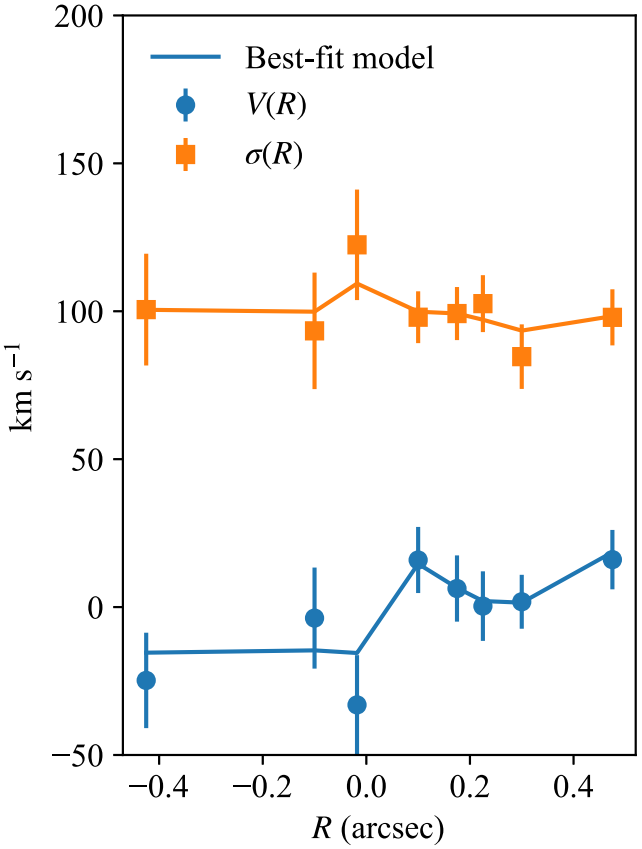

Figure 12. Velocity and velocity dispersion profiles from HST/STIS data and the best-fit model. Although the model is not fit in this space, it is shown to produce a good match to the profiles and demonstrates how the dispersion peak is just off of $R = 0$ with substantial rotation about the center.

observations needs to be considered. Last, we raise a question regarding the quenched nature of NGC 4826 given its recent merger. We discuss each of these in turn below.

5.1. A Low-mass Black Hole Measured with Schwarzschild Modeling

NGC 4826 hosts one of the smallest black holes measured with the stellar dynamical Schwarzschild modeling technique. At $8.4 \times 10^6\,M_\odot$, NGC 4826's black hole is within a factor of 4 of the black hole in NGC 221 (M32), which has mass $M = (2.5 \pm 1.0) \times 10^6\,M_\odot$ (van den Bosch & de Zeeuw 2010), the smallest mass determined by Schwarzschild modeling. There are Schwarzschild modeling results with upper limits below the mass of NGC 221, such as M33 ($M < 1.5 \times 10^3\,M_\odot$ in Gebhardt et al. 2001 and $M < 3 \times 10^3\,M_\odot$ in Merritt et al. 2001) and NGC 205 ($M < 3.8 \times 10^4\,M_\odot$; Valluri et al. 2005). In both of these cases, there is no external evidence for the presence of a black hole so that both of these dynamical results can be interpreted as evidence for absence of a black hole; though, Nguyen et al. (2019) find dynamical evidence for the presence of a black hole in NGC 205 of mass $M = 7^{+96}_{-7} \times 10^3\,M_\odot$.

There are smaller known black holes using other mass estimation techniques, both direct and indirect, including those in NGC 4395 ($M = 4.0^{+8}_{-3} \times 10^5\,M_\odot$ from ionized gas dynamics due to den Brok et al. 2015; 10^4–$10^5\,M_\odot$ from reverberation mapping due to Peterson et al. 2005; Woo et al. 2019), NGC 404 ($M = 5.5^{+4.1}_{-3.8} \times 10^5\,M_\odot$ from molecular gas dynamics due to Davis et al. 2020), Pox 52 ($M \approx 2$–$4 \times 10^5\,M_\odot$ from a variety of indirect methods due to Barth et al. 2004; Thornton et al. 2008), and SDSS J152303.80+114546.0 (RGG 118, $M \sim 5 \times 10^4\,M_\odot$ based on broad emission-line measurements due to Baldassare et al. 2015).

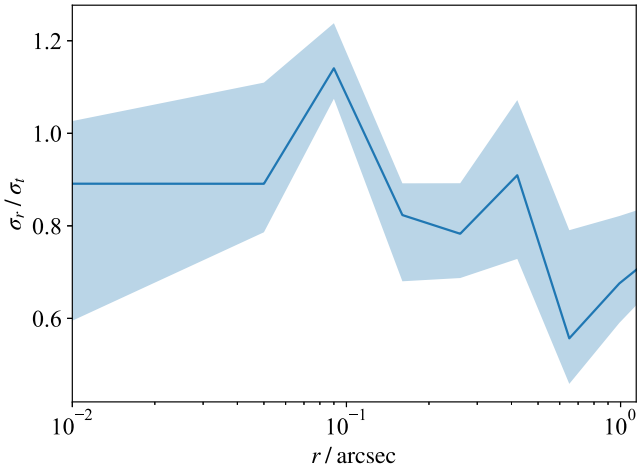

Figure 13. Orbital anisotropy of the models. We plot, as a function of radius, the ratio of radial velocity dispersion to the tangential (azimuthal and polar) velocity dispersion. The solid line is from the best-fit model, and the shaded region comes from the range of values of the 20 best-fit models to estimate the uncertainty. At large radii, the orbits are tangentially biased owing to the disk. At smaller radii, the tangential bias may indicate a depletion of radial orbits from the earlier dynamical activity that produced the counter-rotating gas streams.

Schwarzschild modeling in particular and dynamical modeling in general are sensitive to low-mass black holes, and dynamical mass measurements of black holes are not biased high as has been claimed in the literature. While it is true that—all else equal—smaller black holes are more difficult to detect than larger black holes, the claims that this leads to individual mass estimates and to population estimates being biased to high masses (e.g., Shankar et al. 2016) are not valid. The fact that our modeling sometimes yields upper limits consistent with zero shows that black holes with spheres of influence too small to be resolved will not always result in a false detection of a mass with an implied resolvable sphere of influence (Richstone et al. 2004; Kormendy 2020). While there is the possibility of a publication bias in which upper limits will not be written about, previous analysis has shown that the mass scaling relations and their intrinsic scatter measurements are unlikely to be biased (Gültekin et al. 2011; Kormendy 2020).

5.2. Comparison to Empirical Black Hole Mass Scaling Relations

Here we show that the black hole mass $M = 8.4^{+1.7}_{-0.6} \times 10^6\,M_\odot$, or $\log M = 6.92^{+0.08}_{-0.03}$ in the composite (classical bulge plus pseudobulge) galaxy NGC 4826 is consistent with the black hole–host galaxy correlations separately derived for galaxies that have dominant classical bulges and those that have dominant pseudobulges. Our comparisons are made using bulge properties derived here in Section 2 and the Appendix and the K_s-band mass-to-light ratio $M/L = 0.46$ derived above. The velocity dispersion $\sigma_e = 104\,\mathrm{km\,s^{-1}}$ is calculated from our data as described in Section 3 and Equation (5).

Figure 14 shows the black hole correlations from Kormendy & Ho (2013a). We use these for our main comparison (1) because they omit black holes whose masses are underestimated because the widths of spectral emission lines were

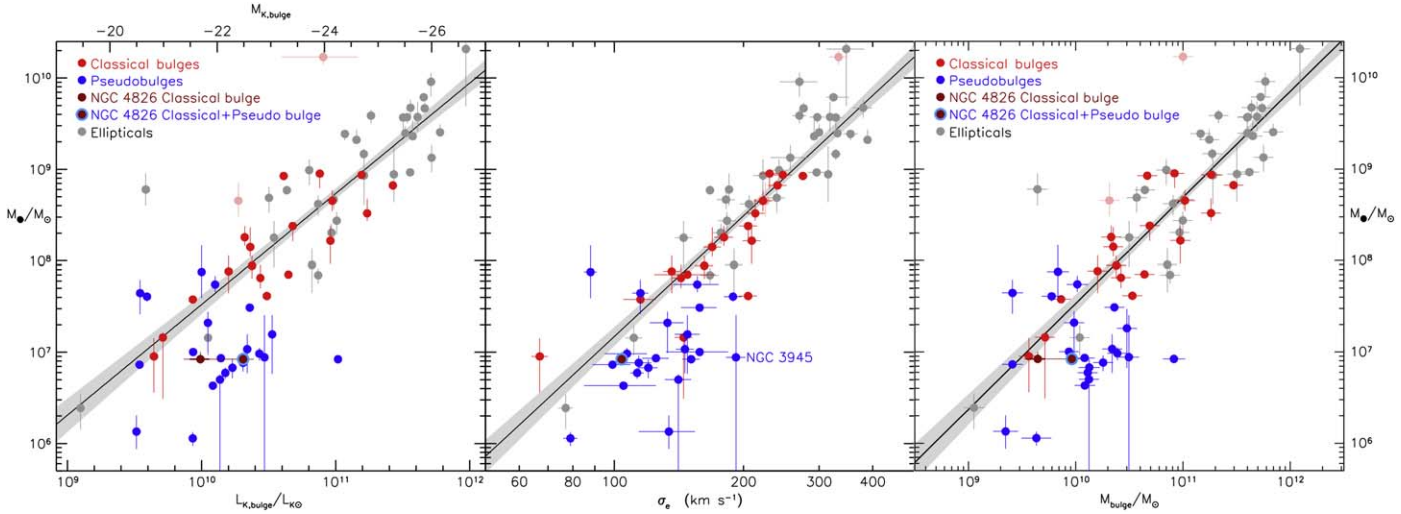

Figure 14. Correlations of black hole mass (here designated $M_\bullet$) with (left) the K_s-band absolute magnitude and luminosity of the bulge component of the galaxy, (center) the bulge velocity dispersion, and (right) the stellar mass of the bulge component. These are the correlations from Kormendy & Ho (2013a) with the preliminary black hole mass for NGC 4826 replaced with the presently derived value and with the point plotted twice, once (dark red) for the adopted classical bulge parameters and again (dark red point surrounded by light blue) for the sum of the classical and pseudobulge. The thick horizontal error bars on the classical bulge points are for the 1σ uncertainty in B/T quoted in Figures 5 and 6. The thin horizontal error bars end at the bulge parameters for the extreme "error bar" decompositions illustrated in the Appendix.

not taken into account in dynamical analyses, (2) because mergers in progress are shown in the above paper to not participate in the correlations and therefore are omitted, (3) because masses measured via stellar dynamics included dark matter halos in most cases, and (4) because the distinction between classical and pseudobulges was measured in the most detail available. So the derived relations were as robust as 2013 data allowed. The scatter in the relations for classical bulges and ellipticals was correspondingly small and essentially the same for all three correlations, 0.29 ± 0.01 dex. Other empirical measurements of black hole mass correlating with host galaxy properties exist (e.g., Kormendy 1993a; Kormendy & Richstone 1995; Magorrian et al. 1998; Ferrarese & Merritt 2000; Gebhardt et al. 2000a; Graham et al. 2001; Tremaine et al. 2002; Marconi & Hunt 2003; Häring & Rix 2004; Hopkins et al. 2007; Graham 2008, 2024; Gültekin et al. 2009b, 2019; Woo et al. 2010; Burkert & Tremaine 2010; Xiao et al. 2011; Beifiori et al. 2012; McConnell & Ma 2013; Sun et al. 2013; Reines & Volonteri 2015; Greene et al. 2016; Saglia et al. 2016; van den Bosch 2016; Davis et al. 2017, 2018, 2019; Sahu et al. 2019a, 2019b, 2022; de Nicola et al. 2019; Kormendy 2020; Bennert et al. 2021; Caglar et al. 2023; Graham & Sahu 2023). We use the Kormendy & Ho (2013a) relation instead of any of the others because of the four points mentioned above. The other measurements are not as useful for furthering understanding about the physics underlying the scaling relations because of one or more of the following: (1) they do not have the same quantity of quality data, (2) they are intended for black hole mass estimation at large distances where even bulge–disk decomposition is difficult, let alone classical–pseudobulge decomposition, and/or (3) they are investigating different physics such as AGN-related scaling relations.

Figure 14 shows that the black hole in NGC 4826 satisfies all three correlations if we use the parameters of the classical bulge part of the galaxy. In the M–bulge luminosity correlation, the classical bulge point lies low but is consistent with the range of the scatter. In the other two correlations, the classical bulge point lies close to the ridge line of the scatter.

The blue points in Figure 14 are for galaxies that have only a pseudobulge or were judged to have a pseudobulge that is substantially more massive than any classical bulge. NGC 4826 was recognized to be a difficult case with comparable classical and pseudobulges. This is consistent with the conclusions of the present paper. Lacking the detailed measurements and analysis of the present work, the galaxy was plotted then as a blue point with a preliminary black hole mass measurement. This has been replaced here with the present data. If we treat NGC 4826 in the same way as the blue points, i.e., if we plot a point at the sum of the classical bulge and pseudobulge luminosity of mass, then that point is low—outside the scatter for the red points—in the correlation with K_s-band luminosity. This point is consistent with the conclusions of Hu (2008), Greene et al. (2010), Kormendy et al. (2011), and Kormendy & Ho (2013a) that pseudobulges contain undermassive black holes—undermassive when compared to the correlation for classical bulges and ellipticals. That is, the blue-plus-red point for NGC 4826 is essentially in the middle of the (uncorrelated) scatter in the blue points.

In the M–σ correlation, black holes in pseudobulges also tend to be undermassive compared to those in classical bulges, but their mean deviation below the classical bulge relation is less than it is for the bulge mass and luminosity correlations. The black hole in NGC 4826 is almost on the ridge line of the correlation for classical bulges and ellipticals, as is the case for many other pseudobulges.

Note in the left-hand parts of Figure 14 that there is very little "room" for the process that made the pseudobulge to have added significantly to the black hole mass. This is consistent with the suggestion in Kormendy & Ho (2013a) that black hole growth has little effect on galaxy evolution for such galaxies.

We can also compare to other published correlations. In contrast to the bulge scaling relations presented above, maser measurements show a broader distribution of masses at fixed galaxy property. Using a sample that includes 20 black holes

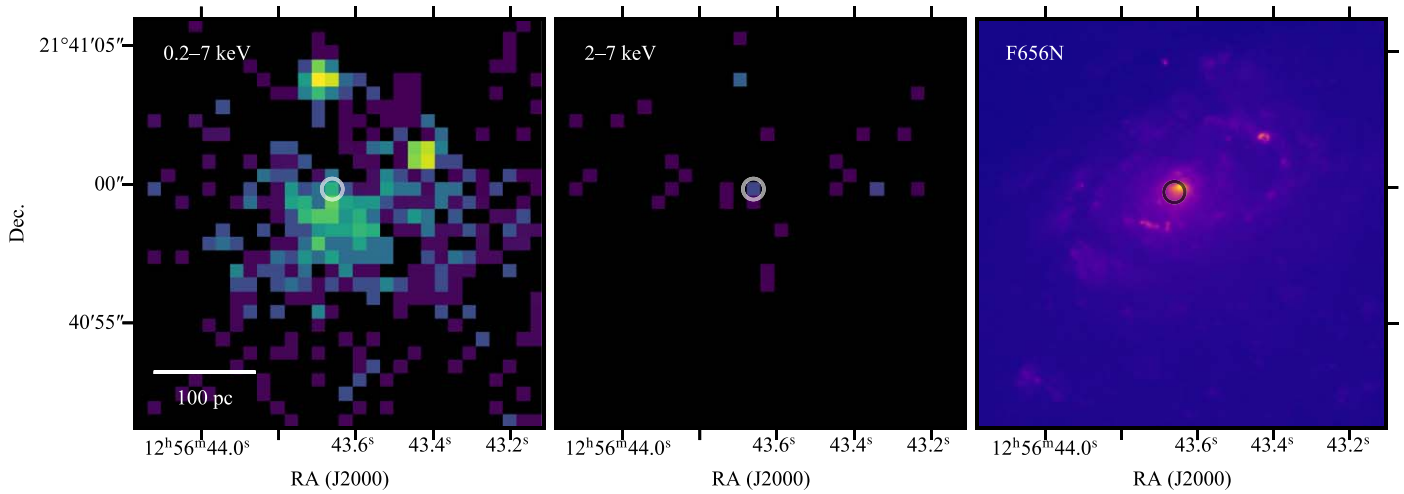

Figure 15. Central 15″ × 15″ of NGC 4826 as observed with Chandra in the 0.2–7 keV band (left), the hard 2–7 keV band (center), and with HST/WFPC2 through the F656N filter. The full band X-ray image shows distinct point sources as well as diffuse emission. The hard band X-ray image shows a relatively small amount of emission coming from the central region, but there is a potential hard X-ray point source (location indicated by a circle in all three panels) that is consistent with the stellar surface brightness peak; though, it requires deeper X-ray imaging to fully assess.

with maser mass estimates, Greene et al. (2016) found an M–σ_* relation for late-type galaxies. The definition of velocity dispersion used by Greene et al. (2016), i.e., σ_*, does not include rotational support so that the corresponding value for NGC 4286 ($\sigma_* = 92$ km s^{-1}) is smaller than our earlier value of σ_e. The predicted mass is $\log M = 6.65 \pm 0.49$, consistent with our mass estimate. It is worth noting that among dynamical mass measurements, the M–σ and M–$L_{\rm bulge}$ relations are poorly populated near NGC 4826's location. In particular, only two galaxies have smaller velocity dispersions than NGC 4826 in the Kormendy & Ho (2013a) sample and only six in the Greene et al. (2016) sample, so that the M–σ relation is necessarily less well measured here.

We also compare to the Reines & Volonteri (2015) relation between the black hole mass of an AGN and the total stellar mass of the host, regardless of the bulge type. Adopting a solar K-band absolute magnitude of $K_\odot = 3.27$ (Willmer 2018), our measured total K-band absolute magnitude of $M_{KT} = -24.06$ for NGC 4826 implies a K-band stellar luminosity $\log(L_T/L_\odot) = 10.93$. Using our estimated $M/L = 0.46$, the total stellar mass is $\log(M_*/M_\odot) = 10.59$. This stellar mass predicts a logarithmic black hole mass of $\log M = 7.02 \pm 0.55$, very close to our measured mass.

5.3. Multiwavelength Evidence for a Black Hole in NGC 4826

Our black hole mass estimate is only marginally consistent with $M = 0$ at the 3σ level, and multiwavelength data support the presence of a mildly accreting black hole. The most compelling indication for an accreting black hole in NGC 4826 comes from optical spectra due to Moustakas et al. (2010). The spectra were taken in a square nuclear region of size 2.″5 as well as at larger angular scales. Although the nuclear spectrum shows no broad Balmer lines, the narrow line ratios indicate the power source of ionizing radiation to be an AGN. The values and uncertainties in [N II]/Hα and [O III]/Hβ allow for the possibility that the lines are driven by a composite AGN and star-forming ionizing radiation field, but it is nominally in the Kewley et al. (2001) AGN region of the Baldwin et al. (1981, BPT) diagram and in any case still requires some contribution from an AGN. A potential complication is that at low luminosities and perhaps especially so for low-mass black holes, it is difficult to identify shock-ionization, which may result from either AGN or from stellar sources (Ho 2008; Eracleous et al. 2010; Molina et al. 2018). Our analysis of the higher spatial resolution STIS emission-line spectrum is mostly in agreement with the results from Moustakas et al. (2010) with even higher [N II]/Hα values (1.45–2.6 depending on the spatial location of the emission, compared to their value of 1.2–1.3) thus increasing the confidence of optical-emission-line identification as an AGN. We finally note that NGC 4826 was also classified as an AGN in Ho et al. (1997).

The X-ray data of NGC 4826 do not strongly argue for an accreting black hole, nor do they present strong evidence against the case. As part of a larger Chandra archival X-ray survey of the Spitzer Infrared Nearby Galaxy Survey, Grier et al. (2011) note that NGC 4826 has a nuclear X-ray point source but that it is unlikely to be AGN emission because of its soft spectrum in a 2 ks observation. Since then, a deeper 30 ks observation was taken and has largely confirmed the picture that the central X-ray emission is dominated by a combination of dimmer X-ray point sources (presumably X-ray binaries) and diffuse emission. We show an image of the Chandra data in Figure 15.

Our analysis of the newer Chandra data, which were also analyzed by Lehmer et al. (2019) as part of a study on the relation between X-ray binary luminosity functions and host galaxy star formation rates, leads us to conclude that the central X-ray emission is dominated by extended, soft X-ray emission at the center with the potential for a hard (2–7 keV) point source at the putative location of the nuclear black hole but with too few counts to be decisive.

We used the Foord et al. (2019) Bayesian AnalYsis of Multiple AGN in X-ray (BAYMAX) code to test for the presence of a point source. We compared two models for the X-ray emission in the central 5″ × 5″ region: (i) a model of uniform, diffuse X-ray emission and (ii) a model with uniform, diffuse X-ray emission plus a point source at some location in the central region. Our analysis strongly prefers the model with a point source, the best-fit location of which has large uncertainties but is consistent with any definition of the optical/infrared center of the galaxy. We note that our ability to

infer the presence of a point source with BAYMAX depends on how well our diffuse emission model matches reality. In this case, it would require a deeper observation to attempt with more sophisticated diffuse emission models. Even if we take our analysis at face value, the presence of an X-ray point source does not necessarily imply the presence of an AGN. The point source could be an X-ray binary (XRB) or a compact knot of gas heated by shocks or other external means (e.g., Foord et al. 2020). Because the uncertainties on the location of the X-ray point source are also comparable to the separation between the dispersion peak and optical surface brightness peak, we do not attempt absolute astrometric calibration between the X-ray and optical imaging. We also analyzed the X-ray spectra of the decomposed diffuse and point-source emission as absorbed power laws and find that the point source is best described as a soft ($\Gamma = 6.1^{+2.4}_{-2.2}$, 3σ uncertainties) power law with modest intrinsic absorption ($N_H = 5.1^{+13.2}_{-3.8} \times 10^{21}\,\mathrm{cm}^{-2}$, 3σ uncertainties). The luminosity of the point source in the 0.5–8 keV band is $L_X = 5.2^{+1.2}_{-2.4} \times 10^{36}$ erg s^{-1} (3σ uncertainties). The point source is notably harder than the best-fit diffuse emission model ($\Gamma = 7.6^{+1.6}_{-2.0}$, 3σ uncertainties) but is still softer than would be expected for AGN emission, and it has a luminosity that is low enough to be an XRB.

In general, it is possible to distinguish low-luminosity X-ray emission in an AGN from X-ray binary emission by using the fundamental plane of black hole accretion (Gültekin et al. 2019), but in the case of NGC 4826, the source of radio emission appears to be stellar. The fundamental plane of black hole accretion relates the mass of the accreting black hole, its X-ray luminosity, and its core radio luminosity. Because the relation is valid over a large range of black hole masses, it can be used to determine whether a given accreting black hole with X-ray and radio emission is an X-ray binary, an intermediate-mass black hole, or a supermassive black hole. NGC 4826 does have a nuclear radio emission measurement from Karl G. Jansky Very Large Array observations at 1.4 GHz of $S_\nu = 103.4$ mJy (Condon et al. 1998). Based on the ratio of far-infrared fluxes to radio fluxes, Condon et al. (2002) concluded that the radio emission was powered by star formation, compromising the utility of the use of the fundamental plane as a mass estimation tool.

Overall, the multiwavelength evidence is mildly supportive of our conclusion that there is a SMBH at the center of NGC 4826, which we measure to be in the range $M = 8.4^{+1.7}_{-0.6} \times 10^6\,M_\odot$ with 68% confidence.

5.4. Relevance to LISA

The relatively small mass of the black hole in NGC 4826 combined with evidence of recent merger activity makes it a prototype for the kinds of sources to which LISA will be sensitive. The gravitational wave frequency of a merging black hole system right before coalescence scales as M^{-1}. So LISA's good sensitivity in the range of $\sim 2 \times 10^{-3}$ to 2×10^{-2} Hz corresponds to a peak mass sensitivity of $\sim 10^6 (1+z)^{-1}\,M_\odot$. Thus the existence of black holes with mass $\sim 10^5$–$10^7\,M_\odot$ at $z = 0$ indicates the potential for high signal-to-noise gravitational wave events with LISA.

In addition to the mere existence of a low-mass black hole, the evidence of merger activity in NGC 4826 demonstrates such black holes may participate in mergers with other black holes. The primary evidence of NGC 4826's interaction is its counter-rotating outer gas disk (Braun et al. 1992) and the presence of inner, leading spiral-arm structure and outer, trailing spiral-arm structure (Walterbos et al. 1994; Rubin 1994). This activity is present despite the isolated environment of NGC 4826. The details of the gas disks likely indicate a low-mass merger and do not resolve the question of whether what has merged with NGC 4826 had a black hole, but it nonetheless increases confidence in the potential for low-mass black holes to merge with others in the local Universe. Confidence in low-mass galaxies to merge is further boosted by the recent analysis of halo stars that show a shell feature and a plume feature that is well interpreted as remnants of a recent merger with a gas-rich galaxy of mass similar to NGC 292 (Smercina et al. 2023).

The evidence of recent merger activity makes NGC 4826 the most recent member of the "mergers in progress" with black hole mass measurement. "Mergers in progress" tend to have undermassive black holes compared to expectations based on galaxy scaling relations (Kormendy & Ho 2013a). The mass we measure for NGC 4826 is smaller than any others identified in Kormendy & Ho (2013a) and the only one consistent with $M < 1 \times 10^7\,M_\odot$ at the 1σ level, though two are just above (NGC 2960: $M = 1.08^{+0.04}_{-0.05} \times 10^7\,M_\odot$; IC 1381: $M = 1.49^{+0.44}_{-0.45} \times 10^7\,M_\odot$).

5.5. Open Questions

A remaining question is why, overall, star formation in NGC 4826 is quenched when it has manifestly accreted a gas-rich companion recently enough so that we still see large amounts of dust and, at large radii, a counter-rotating gas disk. Feedback from AGN activity is unlikely to be the cause of halting star formation. In the context of our M measurement and the black hole correlations, there is little room for any significant addition to the black hole mass via the galaxy accretion event that—we argue—built the pseudobulge.

If we underestimate the black hole mass by a factor of $\sim$2, then there is more room for recent black hole growth and therefore radiative output by an AGN. We offer a few caveats that are, effectively, uncontrollable systematic uncertainties that could conceivably contribute to an underestimated mass. The slight difference in location between the velocity dispersion and surface brightness maxima could be a sign that near-central dust absorption is bigger than we think. We therefore may not see the high-velocity stars that are signatures of a bigger black hole. Additionally, STIS slit centering was carried out at $\sim$8500 Å. In a worst-case scenario, asymmetric dust absorption could result in a slit centering that missed the black hole and thus we only see a diminished effect of a larger black hole. Uncertainty about M may be resolved with ALMA measurements, if there is a molecular gas disk near the center.

6. Summary

We used high-spatial-resolution observations of NGC 4826 to analyze the light distribution and structural parameters of the host as well as to measure the black hole mass and mass-to-light ratio. The imaging data were from HST/WFPC2 in F547M and F656N, 2MASS, NICMOS, WISE, and Spitzer. The spectroscopic data of the nucleus were HST/STIS observations taken of the Ca II triplet and a series of emission lines, combined with HET LRS data of the outer regions of the galaxy. The photometric analysis and decomposition revealed complex morphology with a combination classical bulge and pseudobulge as well as a disk. Our adopted decomposition requires an $n = 3.27$ classical bulge, an $n = 0.58$ partial

pseudobulge, two lens components (an $n = 0.18$ inner lens and an $n = 0.17$ outer lens), and a disk component with $n = 1.07$. We consider the partial pseudobulge and two lens components as the galaxy's pseudobulge. The total V-band luminosity is $M_{VT} = -21.07$, the classical bulge to total ratio is $B/T = 0.12$, the pseudobulge to total ratio is $PB/T = 0.13$, and the disk to total ratio is $D/T = 0.75$.

Our Schwarzschild modeling of the galaxy found the mass-to-light ratio in the K_s band to be $\Upsilon_K = 0.46 \pm 0.03\ M_\odot L_\odot^{-1}$ and the black hole mass to be $M = 8.4^{+1.7}_{-0.6} \times 10^6\ M_\odot$ at our assumed distance of 7.27 Mpc.

Our modeling is only marginally consistent with $M = 0$ at about the 3σ level, and a preponderance of other lines of evidence, including BPT diagnostics of optical emission lines and continuum X-ray emission, leads us to conclude that there is an accreting black hole at the center of NGC 4826.

This black hole mass in NGC 4826 satisfies published scaling relations between M and the K-band luminosity, stellar mass, and velocity dispersion of only the classical bulge part of the galaxy. It is undermassive compared to the sum of the bulge and pseudobulge K-band luminosities. Thus the black hole in NGC 4826 is consistent with published results on scaling relations between black holes and classical and pseudobulges.

The black hole in NGC 4826 is among the smallest to have been measured via orbit superposition modeling of the stellar dynamics. The measurement of such a small black hole mass demonstrates the ability of black hole mass measurements to probe small masses. The presence of a black hole with mass $M \lesssim 10^7\ M_\odot$ in a galaxy with evidence for a recent merger is also promising as an example of low-mass black holes that may merge with other black holes, to which LISA will be sensitive.

Acknowledgments

We thank STScI's Hubble Heritage project for making their images available in the public domain. K. Gültekin thanks Jessie Runnoe for helpful conversations regarding the AGN emission-line spectra. XVISTA is maintained and distributed by Jon Holtzman at New Mexico State University (http://ganymede.nmsu.edu/holtz/xvista). Some of the data presented in this article were obtained from the Mikulski Archive for Space Telescopes (MAST) at the Space Telescope Science Institute. The specific observations analyzed can be accessed via 10.17909/yep1-qr33. We have also made our photometry and LOSVD data available at https://doi.org/10.7302/kr8z-fj98.

This work made use of the following software packages: FORTRAN77, Jupyter (Perez & Granger 2007; Kluyver et al. 2016), matplotlib (Hunter 2007), numpy (Harris et al. 2020), python (Van Rossum & Drake 2009), SM, VISTA (Stover 1988), and IRAF (Tody 1993, 1986). This research has made use of NASA's Astrophysics Data System. Software citation information was aggregated using The Software Citation Station (Wagg & Broekgaarden 2024, 2024).

The authors acknowledge the Texas Advanced Computing Center (TACC) at The University of Texas at Austin for providing computational resources that have contributed to the research results reported within this paper.

J.K. is grateful for the long-term support provided by the Curtis T. Vaughan, Jr. Centennial Chair in Astronomy. We are most sincerely grateful to Mr. and Mrs. Curtis T. Vaughan, Jr., for their many-year support of Texas astronomy. The ground-based spectrum of NGC 4826 was obtained with the Marcario LRS and the Hobby–Eberly Telescope (HET). LRS is named for Mike Marcario of High Lonesome Optics; he made optics for the instrument but died before its completion. LRS is a project of the HET partnership and the Instituto de Astronomía de la Universidad Nacional Autónoma de México. The HET is a project of the University of Texas at Austin, Pennsylvania State University, Stanford University, Ludwig-Maximilians-Universität München, and Georg-August-Universität Göttingen. The HET is named in honor of its principal benefactors, William P. Hobby and Robert E. Eberly.

Facilities: FLWO:2MASS, HET (LRS), HST (NICMOS, STIS, WFPC2), Spitzer, WISE.

Software: FORTRAN77, numpy, matplotlib, sm, Lick VISTA, NOAO IRAF.

Appendix

Figures 16 and 17 illustrate our alternative photometric decompositions of the brightness profile of NGC 4826. Figure 16 has the biggest allowed classical bulge: the pseudobulge has been reduced to the two shelves in the brightness distribution, which reveal themselves to be disky via local maxima in ellipticity ϵ. The rest of the inner component of a two-Sérsic fit is here called the classical bulge. The fit to the profile is acceptable, but the decomposition is implausible, because the disk has a smaller Sérsic index $n_{\rm Disk} = 0.87 \pm 0.04$ than do other disk galaxies and the bulge has a larger Sérsic index than do the bulges of spiral galaxies. In fact, $n_{\rm Bulge} = 4.28 \pm 0.24$ is

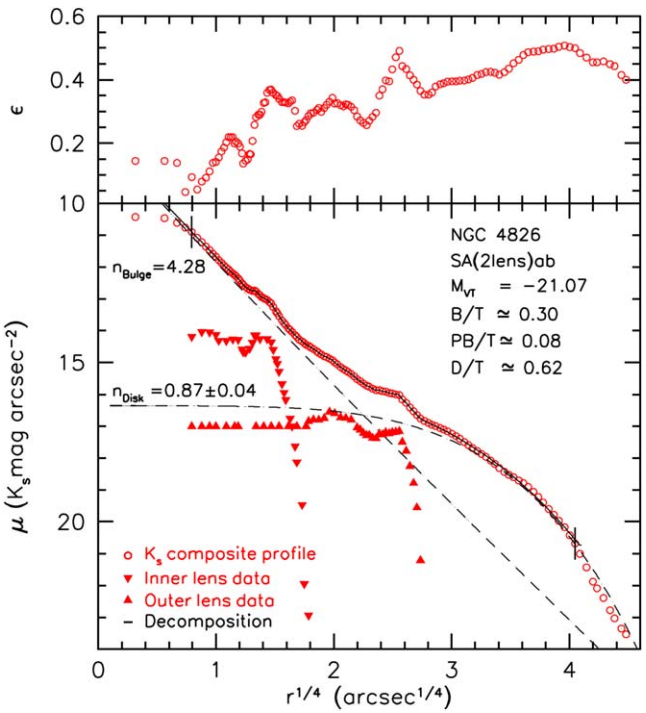

Figure 16. Minimal-pseudobulge photometric decomposition plotted against $(r/\text{arcsec})^{1/4}$ to show components at both small and large radii. Here, the lens components are treated as they are in our adopted fit, and together they are assumed to be all of the pseudobulge. Thus the rest of the profile is decomposed into two Sérsic components to represent a classical bulge and disk. The statistical uncertainties in this fit are small. However, the classical bulge has $n = 4.28$, larger than values normally seen in small bulges, and the disk Sérsic index $n = 0.87 \pm 0.04 < 1$ is smaller than $n = 1$ for an exponential. Data and symbols are the same as in Figure 6.

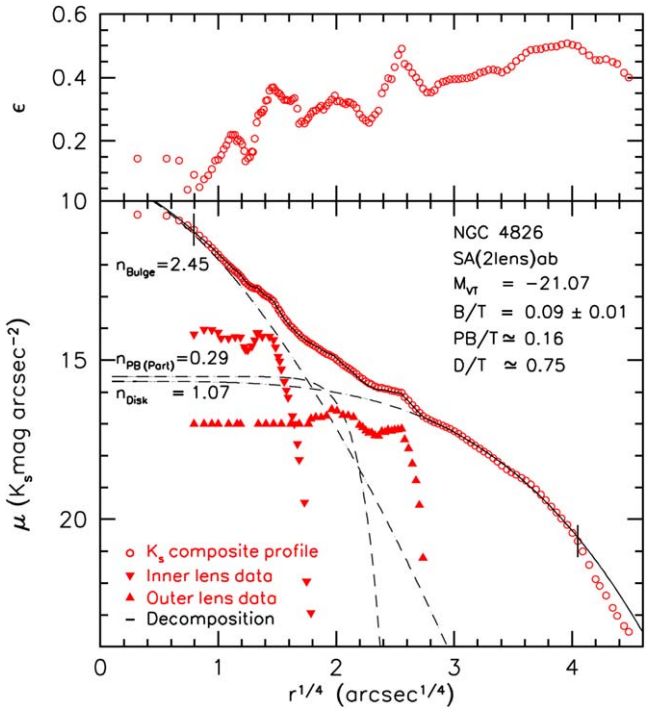

Figure 17. Maximal-pseudobulge photometric decomposition plotted against $(r/\mathrm{arcsec})^{1/4}$ to show components at both small and large radii. In this fit, the parameters were derived to maximize the pseudobulge-to-total ratio PB/T while still producing an acceptable global fit. This procedure required forcing the classical bulge Sérsic index to its lowest value. The lens components are treated as they are in our adopted fit. The classical bulge component contributes roughly half as much light as the pseudobulge, but it still dominates the light inside of $(r/\mathrm{arcsec})^{1/4} = 1.5$. The low classical bulge to total ratio, while not ruled out, is small for an Sab galaxy. Data and symbols are the same as in Figure 6.

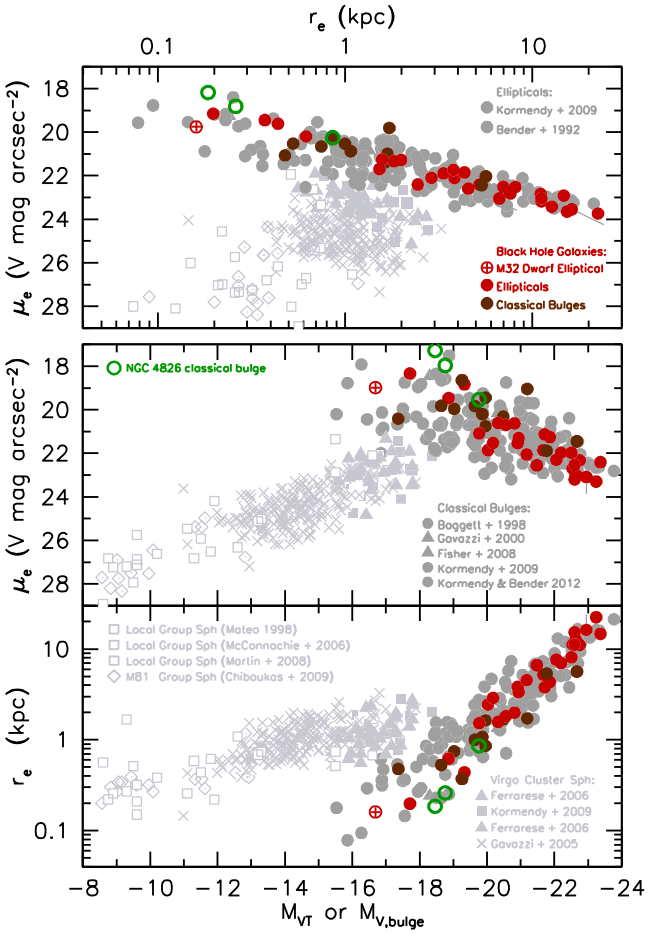

Figure 18. From Kormendy (2020), parameter correlations for elliptical galaxies and classical bulges of disk galaxies (dark gray) and for spheroidal galaxies (light gray). The bottom panels show effective radius r_e that contains half of the total light and effective surface brightness μ_e at r_e correlated with the V-band absolute magnitude of the component. The top panel shows the Kormendy (1977) relation, μ_e vs. r_e; this projection shows the fundamental plane nearly edge-on and has especially small scatter. Sources are given in keys, references omitted here are in Kormendy & Bender (2012). Galaxies in which supermassive black holes are detected via spatially resolved stellar or gas dynamics are encoded in dark red for ellipticals and dark brown for bulges. Our three classical bulge models for NGC 4826 are shown in green; the middle point is for the preferred decomposition.

characteristic of the Sérsic indices $n > 4$ of giant elliptical galaxies with cores (Kormendy et al. 2009).

In contrast, Figure 17 is a fit in which the pseudobulge is constrained to be as luminous as possible. This is done by forcing the classical bulge to have a small Sérsic index, although still one that is consistent with other bulge–disk galaxies.

Note that the maximal (Figure 16), adopted (Figures 5, 6), and minimal (Figure 17) classical bulges all dominate the light of the galaxy in the central few arcsec, i.e., inside and near the sphere-of-influence volume of the black hole.

As discussed in Section 2.3, one test of our photometric component decomposition remains to be carried out. Are the structural parameters of the classical bulge consistent with our understanding of other galaxies? The "fundamental plane" parameter correlations between bulge luminosity, effective radius r_e, and effective brightness μ_e are tight enough for classical bulges so that a meaningful test is possible. In contrast, pseudobulges have larger parameter ranges and are less well studied and understood. So no meaningful test is possible of the pseudobulge parameters that we derive for NGC 4826.

Two structural parameter correlations from Kormendy (2020) are shown in Figures 18 and 19 with the classical bulge parameters of NGC 4826 added. Figure 19 uses data and classifications due to Lauer et al. (2007), Kormendy et al. (2009), and Kormendy & Bender (2013). Kormendy (2020) showed that the structural parameters of those classical bulges and elliptical galaxies in which black holes have been detected via spatially resolved dynamics are entirely normal and sample the complete range of properties observed for classical bulges and ellipticals. This argues against claims (e.g., van den Bosch et al. 2015; van den Bosch 2016; Shankar et al. 2016) that observed correlations between black hole mass and bulge properties are biased because black holes are detected only in a biased subset of galaxies that have especially favorable properties. The only notable exceptions to this are galaxies with $r_e \lesssim 1$ kpc, which have black hole mass measurements only for brighter values of μ_e, and galaxies with $M_{V,\mathrm{bulge}}$ or $M_{VT} > -20$, which have black hole mass measurements for brighter values of μ_e and/or smaller values of r_e.

Here, we see that the bulge models of NGC 4826 lie within the scatter of the correlations for bulges and elliptical galaxies. Actually, the bulge of NGC 4826 is more compact than typical bulges. The smallest bulge is weakly disfavored by the Figure 18 correlations. But overall, the bulge of this galaxy

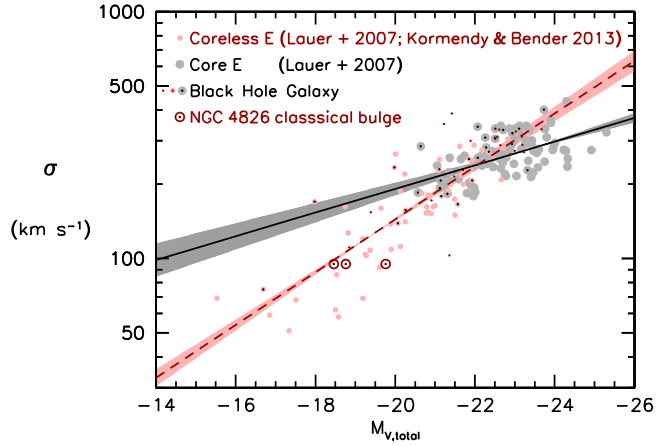

Figure 19. Faber & Jackson (1976) correlations for ellipticals with and without a "core," i.e., a break in the density profile near the center from a steep outer profile to a shallow inner cusp. Total absolute magnitudes and velocity dispersions are from Lauer et al. (2007) with classification corrections from Kormendy et al. (2009) and Kormendy & Bender (2013). Galaxies with dynamical black hole detections are labeled. The lines are symmetric least-squares fits (Tremaine et al. 2002) to the core galaxies (black line with gray 1σ uncertainty) and the coreless galaxies (red line with pink 1σ uncertainty). The kink at $\sigma \simeq 250$ km s^{-1} was also emphasized by Lauer et al. (2007). This figure is from Kormendy (2020) with the three classical bulge models for NGC 4826 added. All are consistent with the correlation for coreless ellipticals. The smaller bulges are slightly favored.

is essentially normal for its M_V, in terms of the correlations between r_e, μ_e, and M_V.

Note that a black hole is successfully detected in NGC 4826, at the compact extreme of the distribution of bulge properties, and in M32, more nearly at the diffuse side of the scatter of bulge properties, both at the low-luminosity end of the parameter correlations.

The same is true for the Faber–Jackson (1976) correlation between M_V and the velocity dispersion σ_* outside the sphere-of-influence radius of the black hole. Core and coreless galaxies have different Faber–Jackson relations (Lauer et al. 2007; Kormendy & Bender 2013), just as they have different Sérsic indices (e. g., Kormendy et al. 2009). But all three bulge models for NGC 4826 are consistent with the Faber–Jackson relation for similar-luminosity coreless ellipticals. The largest-bulge model is slightly disfavored but not excluded.

ORCID iDs

Kayhan Gültekin https://orcid.org/0000-0002-1146-0198
Karl Gebhardt https://orcid.org/0000-0002-8433-8185
John Kormendy https://orcid.org/0000-0001-9854-5217
Adi Foord https://orcid.org/0000-0002-1616-1701
Ralf Bender https://orcid.org/0000-0001-7179-0626
Tod R. Lauer https://orcid.org/0000-0003-3234-7247
Jason Pinkney https://orcid.org/0000-0002-6863-5630
Scott Tremaine https://orcid.org/0000-0002-0278-7180

References

Amaro-Seoane, P., Andrews, J., Arca Sedda, M., et al. 2023, LRR, 26, 2
Baldassare, V. F., Reines, A. E., Gallo, E., & Greene, J. E. 2015, ApJL, 809, L14
Baldwin, J. A., Phillips, M. M., & Terlevich, R. 1981, PASP, 93, 5
Barnes, J. E., & Hernquist, L. 1992, ARA&A, 30, 705
Barth, A. J., Ho, L. C., Rutledge, R. E., & Sargent, W. L. W. 2004, ApJ, 607, 90
Beifiori, A., Courteau, S., Corsini, E. M., & Zhu, Y. 2012, MNRAS, 419, 2497
Bender, R., Burstein, D., & Faber, S. M. 1992, ApJ, 399, 462
Bender, R., Burstein, D., & Faber, S. M. 1993, ApJ, 411, 153
Bender, R., Kormendy, J., Cornell, M. E., & Fisher, D. B. 2015, ApJ, 807, 56
Bennert, V. N., Treu, T., Ding, X., et al. 2021, ApJ, 921, 36
Binney, J., & de Vaucouleurs, G. 1981, MNRAS, 194, 679
Blakeslee, J. P., Jordán, A., Mei, S., et al. 2009, ApJ, 694, 556
Braun, R., Walterbos, R. A. M., & Kennicutt, R. C., J. 1992, Natur, 360, 442
Burkert, A., & Tremaine, S. 2010, ApJ, 720, 516
Caglar, T., Koss, M. J., Burtscher, L., et al. 2023, ApJ, 956, 60
Cappellari, M. 2016, ARA&A, 54, 597
Cappellari, M., Verolme, E. K., van der Marel, R. P., et al. 2002, ApJ, 578, 787
Condon, J. J., Cotton, W. D., & Broderick, J. J. 2002, AJ, 124, 675
Condon, J. J., Cotton, W. D., Greisen, E. W., et al. 1998, AJ, 115, 1693
Cutri, R. M., Skrutskie, M. F., Van Dyk, S., et al. 2003, Explanatory Supplement to the 2MASS All Sky Data Release and Extended Mission Products, https://old.ipac.caltech.edu/2mass/releases/allsky/doc/explsup.html
Davis, B. L., Graham, A. W., & Cameron, E. 2018, ApJ, 869, 113
Davis, B. L., Graham, A. W., & Cameron, E. 2019, ApJ, 873, 85
Davis, B. L., Graham, A. W., & Seigar, M. S. 2017, MNRAS, 471, 2187
Davis, T. A., Nguyen, D. D., Seth, A. C., et al. 2020, MNRAS, 496, 4061
de Blok, W. J. G., Walter, F., Brinks, E., et al. 2008, AJ, 136, 2648
de Nicola, S., Marconi, A., & Longo, G. 2019, MNRAS, 490, 600
de Vaucouleurs, G. 1959, HDP, 53, 275
de Vaucouleurs, G., de Vaucouleurs, A., Corwin, H. G., Jr., et al. 1991, Third Reference Catalogue of Bright Galaxies (Berlin: Springer)
de Zeeuw, T., & Franx, M. 1991, ARA&A, 29, 239
den Brok, M., Seth, A. C., Barth, A. J., et al. 2015, ApJ, 809, 101
Djorgovski, G. S. 1992, in Morphological and Physical Classification of Galaxies (Astrophysics and Space Science Library) Vol. 178 ed. G. Longo, M. Capaccioli, & G. Busarello (Dordrecht: Kluwer), 337
Djorgovski, S., & Davis, M. 1987, ApJ, 313, 59
Djorgovski, S., de Carvalho, R., & Han, M. S. 1988, in ASP Conf. Ser. 4, The Extragalactic Distance Scale, ed. S. van den Bergh & C. J. Pritchet (San Francisco, CA: ASP), 329
Dressler, A. 1989, in IAU Symp. 134, Active Galactic Nuclei, ed. D. E. Osterbrock & J. S. Miller (Dordrecht: Kluwer), 217
Dressler, A., Lynden-Bell, D., Burstein, D., et al. 1987, ApJ, 313, 42
Emsellem, E., Monnet, G., & Bacon, R. 1994, A&A, 285, 723
Eracleous, M., Hwang, J. A., & Flohic, H. M. L. G. 2010, ApJ, 711, 796
Erwin, P., Beltrán, J. C. V., Graham, A. W., & Beckman, J. E. 2003, ApJ, 597, 929
Erwin, P., Saglia, R. P., Fabricius, M., et al. 2015, MNRAS, 446, 4039
Faber, S. M., Dressler, A., Davies, R. L., et al. 1987, in Nearly Normal Galaxies. From the Planck Time to the Present, ed. S. M. Faber (New York: Springer-Verlag), 175
Faber, S. M., & Jackson, R. E. 1976, ApJ, 204, 668
Fazio, G. G., Hora, J. L., Allen, L. E., et al. 2004, ApJS, 154, 10
Ferrarese, L., & Merritt, D. 2000, ApJL, 539, L9
Finkbeiner, D. P., Schlegel, D. J., & Davis, M. 1998, in IAU Colloq. 166, The Local Bubble and Beyond, ed. D. Breitschwerdt, M. J. Freyberg, & J. Truemper, Vol. 506 (Berlin: Springer), 367
Fisher, D. B., & Drory, N. 2011, ApJL, 733, L47
Foord, A., Gültekin, K., Nevin, R., et al. 2020, ApJ, 892, 29
Foord, A., Gültekin, K., Reynolds, M. T., et al. 2019, ApJ, 877, 17
Gebhardt, K., Richstone, D., Ajhar, E. A., et al. 1996, AJ, 112, 105
Gebhardt, K., Bender, R., Bower, G., et al. 2000a, ApJL, 539, L13
Gebhardt, K., Richstone, D., Kormendy, J., et al. 2000b, AJ, 119, 1157
Gebhardt, K., Lauer, T. R., Kormendy, J., et al. 2001, AJ, 122, 2469
Gebhardt, K., Richstone, D., Tremaine, S., et al. 2003, ApJ, 583, 92
Graham, A. W. 2008, ApJ, 680, 143
Graham, A. W. 2024, MNRAS, 531, 230
Graham, A. W., Erwin, P., Caon, N., & Trujillo, I. 2001, ApJL, 563, L11
Graham, A. W., & Sahu, N. 2023, MNRAS, 520, 1975
Greene, J. E., Peng, C. Y., Kim, M., et al. 2010, ApJ, 721, 26
Greene, J. E., Seth, A., Kim, M., et al. 2016, ApJL, 826, L32
Grier, C. J., Mathur, S., Ghosh, H., & Ferrarese, L. 2011, ApJ, 731, 60
Gültekin, K., King, A. L., Cackett, E. M., et al. 2019, ApJ, 871, 80
Gültekin, K., Tremaine, S., Loeb, A., & Richstone, D. O. 2011, ApJ, 738, 17
Gültekin, K., Richstone, D. O., Gebhardt, K., et al. 2009a, ApJ, 695, 1577
Gültekin, K., Richstone, D. O., Gebhardt, K., et al. 2009b, ApJ, 698, 198
Häring, N., & Rix, H.-W. 2004, ApJL, 604, L89
Harris, C. R., Millman, K. J., van der Walt, S. J., et al. 2020, Natur, 585, 357
Hill, G. J., Nicklas, H. E., MacQueen, P. J., et al. 1998, Proc. SPIE, 3355, 375
Ho, L. C. 2008, ARA&A, 46, 475
Ho, L. C., Filippenko, A. V., & Sargent, W. L. W. 1997, ApJS, 112, 315

Hopkins, P. F., Hernquist, L., Cox, T. J., Robertson, B., & Krause, E. 2007, ApJ, 669, 67
Hu, J. 2008, MNRAS, 386, 2242
Hunter, J. D. 2007, CSE, 9, 90
Jarrett, T. H., Chester, T., Cutri, R., et al. 2000, AJ, 119, 2498
Jarrett, T. H., Chester, T., Cutri, R., Schneider, S. E., & Huchra, J. P. 2003, AJ, 125, 525
Kewley, L. J., Dopita, M. A., Sutherland, R. S., Heisler, C. A., & Trevena, J. 2001, ApJ, 556, 121
Kluyver, T., Ragan-Kelley, B., Pérez, F., et al. 2016, in Positioning and Power in Academic Publishing: Players, Agents and Agendas, ed. F. Loizides & B. Schmidt (Amsterdam: IOS Press), 87
Kormendy, J. 1977, ApJ, 218, 333
Kormendy, J. 1978, Brightness Distributions in Compact and Normal Galaxies (Ann Arbor, MI: Univ. Microfilms)
Kormendy, J. 1979, ApJ, 227, 714
Kormendy, J. 1981, in Structure and Evolution of Normal Galaxies, ed. S. M. Fall & D. Lynden-Bell (Cambridge: Cambridge Univ. Press), 85
Kormendy, J. 1984, ApJ, 286, 116
Kormendy, J. 1985, ApJ, 295, 73
Kormendy, J. 1987, in Nearly Normal Galaxies. From the Planck Time to the Present, ed. S. M. Faber (New York: Springer-Verlag), 163
Kormendy, J. 1993a, in The Nearest Active Galaxies, ed. J. Beckman, L. Colina, & H. Netzer (Madrid: Consejo Superior de Investigaciones Cientificas), 197
Kormendy, J. 1993b, IAU Symposium, Vol. 153, Galactic Bulges, ed. H. Dejonghe & H. J. Habing (Dordrecht: Kluwer Academic Publishers), 209
Kormendy, J. 2013, in Secular Evolution in Disk Galaxies, ed. J. Falcón-Barroso & J. H. Knapen (Cambridge: Cambridge Univ. Press), 1
Kormendy, J. 2015, HiA, 16, 316
Kormendy, J. 2016, in Galactic Bulges (Astrophysics and Space Science Library) Vol. 418 ed. R. Peletier & D. Gadotti (New York: Springer), 431
Kormendy, J. 2020, in IAU Symp. 353, Galactic Dynamics in the Era of Large Surveys, ed. M. Valluri & J. A. Sellwood (Cambridge: Cambridge Univ. Press), 186
Kormendy, J., & Bender, R. 2009, ApJL, 691, L142
Kormendy, J., & Bender, R. 2012, ApJS, 198, 2
Kormendy, J., & Bender, R. 2013, ApJL, 769, L5
Kormendy, J., Bender, R., & Cornell, M. E. 2011, Natur, 469, 374
Kormendy, J., & Djorgovski, S. 1989, ARA&A, 27, 235
Kormendy, J., Drory, N., Bender, R., & Cornell, M. E. 2010, ApJ, 723, 54
Kormendy, J., Fisher, D. B., Cornell, M. E., & Bender, R. 2009, ApJS, 182, 216
Kormendy, J., & Ho, L. C. 2013a, ARA&A, 51, 511
Kormendy, J., & Ho, L. C. 2013b, arXiv:1308.6483
Kormendy, J., & Kennicutt, R. C. J. 2004, ARA&A, 42, 603
Kormendy, J., & Richstone, D. 1995, ARA&A, 33, 581
Kuo, C. Y., Braatz, J. A., Condon, J. J., et al. 2011, ApJ, 727, 20
Lauer, T. R. 1985, ApJS, 57, 473
Lauer, T. R., Faber, S. M., Richstone, D., et al. 2007, ApJ, 662, 808
Lehmer, B. D., Eufrasio, R. T., Tzanavaris, P., et al. 2019, ApJS, 243, 3
Magorrian, J., Tremaine, S., Richstone, D., et al. 1998, AJ, 115, 2285
Marconi, A., & Hunt, L. K. 2003, ApJL, 589, L21
Mathis, J. S. 2000, in Circumstellar and Interstellar Material, ed. A. N. Cox (4th ed.; New York: Springer), 523
McConnell, N. J., & Ma, C.-P. 2013, ApJ, 764, 184
Merritt, D., Ferrarese, L., & Joseph, C. L. 2001, Sci, 293, 1116
Mihos, J. C., & Hernquist, L. 1994, ApJL, 437, L47
Molina, M., Eracleous, M., Barth, A. J., et al. 2018, ApJ, 864, 90
Monnet, G., Bacon, R., & Emsellem, E. 1992, A&A, 253, 366
Moustakas, J., Kennicutt, R. C. J., Tremonti, C. A., et al. 2010, ApJS, 190, 233
Nguyen, D. D., Seth, A. C., Neumayer, N., et al. 2019, ApJ, 872, 104
Nowak, N., Saglia, R. P., Thomas, J., et al. 2008, MNRAS, 391, 1629
Perez, F., & Granger, B. E. 2007, CSE, 9, 21
Persic, M., Salucci, P., & Stel, F. 1996, MNRAS, 281, 27
Peterson, B. M., Bentz, M. C., Desroches, L.-B., et al. 2005, ApJ, 632, 799
Pinkney, J., Gebhardt, K., Bender, R., et al. 2003, ApJ, 596, 903
Reines, A. E., & Volonteri, M. 2015, ApJ, 813, 82
Richstone, D., Gebhardt, K., Aller, M., et al. 2004, arXiv:ph/0403257
Rix, H.-W. R., Kennicutt, R. C. J., Braun, R., & Walterbos, R. A. M. 1995, ApJ, 438, 155
Romanowsky, A. J., & Kochanek, C. S. 1997, MNRAS, 287, 35
Rubin, V. C. 1994, AJ, 107, 173
Saglia, R. P., Opitsch, M., Erwin, P., et al. 2016, ApJ, 818, 47
Sahu, N., Graham, A. W., & Davis, B. L. 2019a, ApJ, 876, 155
Sahu, N., Graham, A. W., & Davis, B. L. 2019b, ApJ, 887, 10
Sahu, N., Graham, A. W., & Davis, B. L. 2022, ApJ, 927, 67
Sandage, A. 1961, The Hubble Atlas of Galaxies
Sandage, A., & Bedke, J. 1994, The Carnegie atlas of galaxies, Vol. 638
Sandage, A., Freeman, K. C., & Stokes, N. R. 1970, ApJ, 160, 831
Savorgnan, G. A. D., Graham, A. W., Marconi, A., & Sani, E. 2016, ApJ, 817, 21
Schwarzschild, M. 1979, ApJ, 232, 236
Sellwood, J. A. 2014, RvMP, 86, 1
Sérsic, J. L. 1968, Atlas de Galaxias Australes (Córdoba: Observatorio Astronómico)
Shankar, F., Bernardi, M., Sheth, R. K., et al. 2016, MNRAS, 460, 3119
Siopis, C., Gebhardt, K., Lauer, T. R., et al. 2009, ApJ, 693, 946
Smercina, A., Bell, E. F., Price, P. A., et al. 2023, ApJL, 949, L37
Stover, R. J. 1988, in Instrumentation for Ground-Based Optical Astronomy, 443 ed. L. B. Robinson (New York: Springer), 443
Sun, A.-L., Greene, J. E., Impellizzeri, C. M. V., et al. 2013, ApJ, 778, 47
Thornton, C. E., Barth, A. J., Ho, L. C., Rutledge, R. E., & Greene, J. E. 2008, ApJ, 686, 892
Tody, D. 1986, Proc. SPIE, 627, 733
Tody, D. 1993, in ASP Conf. Ser. 52, Astronomical Data Analysis Software and Systems II, ed. R. J. Hanisch, R. J. V. Brissenden, & J. Barnes (San Francisco, CA: ASP), 173
Tonry, J. L., Dressler, A., Blakeslee, J. P., et al. 2001, ApJ, 546, 681
Toomre, A. 1977, in Evolution of Galaxies and Stellar Populations, ed. B. M. Tinsley et al., 401
Tremaine, S. 1989, in Dynamics of Astrophysical Discs, ed. J. A. Sellwood, 231
Tremaine, S., Gebhardt, K., Bender, R., et al. 2002, ApJ, 574, 740
Valluri, M., Ferrarese, L., Merritt, D., & Joseph, C. L. 2005, ApJ, 628, 137
van den Bosch, R. C. E. 2016, ApJ, 831, 134
van den Bosch, R. C. E., & de Zeeuw, P. T. 2010, MNRAS, 401, 1770
van den Bosch, R. C. E., Gebhardt, K., Gültekin, K., et al. 2012, Natur, 491, 729
van den Bosch, R. C. E., Gebhardt, K., Gültekin, K., Yıldırım, A., & Walsh, J. L. 2015, ApJS, 218, 10
van Driel, W., & Buta, R. 1993, PASJ, 45, L47
Van Rossum, G., & Drake, F. L. 2009, Python 3 Reference Manual (Scotts Valley, CA: CreateSpace),
Verolme, E. K., Cappellari, M., Copin, Y., et al. 2002, MNRAS, 335 517
Wagg, T., & Broekgaarden, F. 2024, The Software Citation Station, Zenodo, doi:10.5281/zenodo.11292917
Wagg, T., & Broekgaarden, F. S. 2024, arXiv:2406.04405
Walterbos, R. A. M., Braun, R., & Kennicutt, R. C., J. 1994, AJ, 107, 184
Werner, M. W., Roellig, T. L., Low, F. J., et al. 2004, ApJS, 154, 1
Willmer, C. N. A. 2018, ApJS, 236, 47
Wirth, A., & Gallagher, J. S. I. 1984, ApJ, 282, 85
Woo, J., Treu, T., Barth, A. J., et al. 2010, ApJ, 716, 269
Woo, J.-H., Cho, H., Gallo, E., et al. 2019, NatAs, 3, 755
Wright, E. L., Eisenhardt, P. R. M., Mainzer, A. K., et al. 2010, AJ, 140, 1868
Xiao, T., Barth, A. J., Greene, J. E., et al. 2011, ApJ, 739, 28